

PASSIVE WIRELESS ANTENNA SENSORS FOR CRACK  
DETECTION AND SHEAR/COMPRESSION SENSING

by

IRSHAD MOHAMMAD

Presented to the faculty of the Graduate School of  
The University of Texas at Arlington in partial fulfillment  
of the Requirements  
for the Degree of

DOCTOR OF PHILOSOPHY

THE UNIVERSITY OF TEXAS AT ARLINGTON

August 2012

Copyright © by Irshad Mohammad 2012

All Rights Reserved

## ACKNOWLEDGEMENTS

I am grateful to the Almighty for giving me the opportunity to be part of the US educational system. I am also thankful to my thesis advisor Dr. Haiying Huang for accepting me as a member of the Advanced Sensor Technology Laboratory (ASTL). It was a nice experience working at ASTL. I am also thankful to my advisor for providing financial support during the five years of my doctoral program.

I would like to extend my thanks to Dr. Wen Chan, Dr. Kamesh Subbarao, Dr. Alan Bowling and Dr. Tjuatja Saibun for serving in my thesis committee.

Special thanks to all my graduate and undergraduate colleagues for their help and well wishes. I would also like to thank Mr. Kermit Beird for his help and assistance at the machine shop.

Last but not the least; I would like to thank all my family members for their love, affection, care and support.

July 6, 2012

## ABSTRACT

### PASSIVE WIRELESS ANTENNA SENSORS FOR CRACK DETECTION AND SHEAR/COMPRESSION SENSING

Irshad Mohammad, PhD

The University of Texas at Arlington, 2012

Supervising Professor: Haiying Huang

Despite the fact that engineering components and structures are carefully designed against fatigue failures, 50 to 90% of mechanical failures are due to fatigue crack formation. The severity of the failure depends on both the crack length and its orientation with respect to the loading direction. Many types of sensors are available that can detect fatigue crack propagation. But, crack orientation detection has been rarely reported in the literature. We evaluated a patch antenna sensor capable of detecting crack propagation as well as crack orientation changes. The aim of the sensors would be to evaluate the real-time health condition of metallic structures to avoid catastrophic failures. The proposed crack sensing system consists of a dielectric substrate with a ground plane on one side of the substrate and an antenna patch printed on the other side of the substrate. The ground plane and the antenna patch, both

conductive in nature, form an electromagnetic resonant cavity that radiates at distinct frequencies. The frequencies are monitored to evaluate the condition of cracks. A wireless sensor array can be realized by implementing a wireless interrogation unit. The scientific merits of this research are: 1) high sensitivity: it was demonstrated that the antenna sensors can detect crack growth with a sub-millimeter resolution; 2) passive wireless operation: based on microstrip antennas, the antenna sensors encode the sensing information in the backscattered antenna signal and thus can transmit the information without needing a local battery; 3) thin and conformal: the entire sensor unit is less than a millimeter thick and highly conformal; 4) crack orientation detection: the crack orientation on the structure can be precisely evaluated based on a single parameter, which only few sensors can accomplish.

In addition to crack detection, the patch antenna sensors are also investigated for measuring shear and pressure forces, with an aim to study the formation, diagnostics and prevention of foot ulcers in diabetic patients. The scientific merits of this proposed research are: 1) simultaneous shear/pressure measurement: current smart shoe technology can only measure shear and pressure separately due to the size of the shear sensor. The proposed sensor can measure shear and pressure deformation simultaneously; 2) high sensitivity and spatial resolution: these sensors are very sensitive and have compact size that enables measuring stress distribution with fine spatial resolution.

## TABLE OF CONTENTS

ACKNOWLEDGEMENTS.....	iii
ABSTRACT .....	iv
LIST OF ILLUSTRATIONS.....	viii
Chapter	Page
1. INTRODUCTION.....	1
1.1 Crack Detection Sensor .....	2
1.2 Shear/compression Sensor .....	6
1.3 Advantages of the Proposed Sensor .....	10
1.4 Thesis Indexing.....	10
2. MICROSTRIP ANTENNA DESIGN .....	12
2.1 Introduction.....	12
2.2 Antenna Modeling .....	15
3. CRACK DETECTION USING PATCH ANTENNA .....	19
3.1 Proposed Crack Detection Sensor .....	19
3.2 Improving the Reliability of Antenna Sensor .....	29
3.3 Crack Orientation Detection .....	35
3.4 Wireless Interrogation of Hidden Cracks .....	48
4. SHEAR/COMPRESSION SENSING .....	54

4.1 Shear Detection Sensor .....	54
4.2 Pressure Detection Sensor .....	61
4.3 Implementation of Hybrid Sensor inside Shoe .....	66
5. CONCLUDING REMARKS.....	70
5.1 Crack Detection .....	70
5.2 Shear/compression Detection .....	71
6. FUTURE WORK.....	72
REFERENCES .....	73
BIOGRAPHICAL INFORMATION.....	83

## LIST OF ILLUSTRATIONS

Figure	Page
2.1 Schematic of microstrip patch antenna; (a) patch antenna; (b) current directions in the patch; (c) $S_{11}$ parameters of a patch antenna .....	13
2.2 S-parameter illustration; (a) power reflected at spectacles; (b) two port network.....	14
2.3 (a) Electric field lines on a patch antenna (side view); (b) top view showing tangential fringing electric fields that are responsible for radiation .....	15
3.1 Principle of antenna sensor for crack detection; (a) & (b) antenna sensor with a crack along its length and its effect on the $f_{10}$ frequency; (c) & (d) antenna sensor with a crack along its width and its effect on the $f_{01}$ frequency; (e) & (f) antenna sensor with an inclined crack and its effect on both $f_{10}$ and $f_{01}$ frequencies .....	20
3.2 Design of CT specimen .....	23
3.3 (a) antenna sensor/SMA assembly; (b) reference marks on the back side of the specimen .....	25
3.4 Experimental setup for fatigue testing.....	26
3.5 Effect of crack growth on $f_{10}$ frequency of antenna sensor; (a) shift of $S_{11}$ curves with crack growth; (b) $f_{10}$ frequency vs. crack tip location .....	27
3.6 Effect of crack growth on $f_{01}$ frequency of antenna sensor at 300 lbs; (a) $S_{11}$ curves at different crack tip locations; (b) $f_{01}$ frequency vs. crack tip location; (c) current density pattern of $TM_{01}$ radiation mode.....	29
3.7 Simulation model; (a) Kapton layer bonded on both	

	sides of the specimen; (b) meshing of the simulation model.....	30
3.8	Strain transfer from specimen to Kapton; (a) without PDMS layer; (b) with PDMS layers of different thickness .....	32
3.9	Measures $S_{11}$ parameters of the fabricated antenna sensor .....	33
3.10	Effect of PDMS on crack-induced frequency shift of the antenna sensor; (a) $f_{10}$ frequency shift at various crack lengths; (b) frequency shift vs. crack tip locations.....	34
3.11	Fixture for crack propagation and monitoring; (a) SMA/patch antenna sensor assembly; (b) reference marks on the ground plane of the antenna sensor .....	36
3.12	SuperScribe circuit prototyping system.....	37
3.13	Crack configurations; (a) crack parallel to the length and at a distance $d$ from center line; (b) crack along the diagonal of the patch; (c) cracks at various inclination angles; (d) kinked cracks.....	39
3.14	(a) simulation model of the patch antenna in HFSS <sup>®</sup> ; (b) design of Patch antenna sensor (All dimensions are in mm).....	40
3.15	Effect of a crack passing perpendicular to the width at an offset to the center of the patch; (a) crack configuration; (b) shift of $S_{11}$ curves with crack growth; (c) experimental and simulated $f_{10}$ and $f_{01}$ frequencies at different crack tip locations; (d) effect of crack offset on the resonant frequency shift; (e) current distribution along $TM_{10}$ radiation mode .....	42
3.16	Effect of diagonal crack on the antenna sensor; (a) crack configuration; (b) $f_{10}$ resonant frequency shift vs. crack tip locations; (c) $f_{01}$ resonant frequency shift vs. crack tip locations; (d) $TM_{10}$ mode current distribution with a diagonal crack; (e) $TM_{01}$ mode current distribution with a diagonal crack.....	43
3.17	Effect of various inclination angles on antenna frequency; (a) schematic of crack propagation; (b) frequency ratio	

	vs. crack tip locations .....	45
3.18	Effect of crack kinking on the antenna frequency; (a) schematic of crack propagation; (b) freq. ratio vs. crack tip locations .....	46
3.19	Patch antenna sensor and the data acquisition system.....	48
3.20	(a) & (b) time and frequency domain representation of the backscattered signal when the interrogation frequency is close to the antenna resonant frequency; (d)&(e) time and frequency domain representation of the backscattered signal when the interrogation frequency is away from the antenna resonant frequency.....	50
3.21	Experimental setup for remote interrogation of antenna sensor .....	52
3.22	Effect of crack propagation on the resonant frequency of the antenna sensor; (a) shift of peak power with crack propagation; (b) normalized resonant frequency shift versus crack tip location .....	53
4.1	HFSS simulation model of the shear sensor .....	55
4.2	Simulated relationship between overlapping length and antenna frequency .....	57
4.3	Antenna shear sensor; (a) poron substrate sandwiched between the antenna patch and the ground plane – side view; (b) SMA/patch assembly with the antenna patch shown – top view .....	57
4.4	Experiment setup for shear sensing .....	58
4.5	Effect of shear displacement on the resonant frequency of the antenna sensor; (a) shift of $S_{11}$ curves with shear displacement; (b) resonant frequency shift vs. shear displacement .....	59
4.6	Principle of loop antenna sensor for pressure detection; (a) schematic of loop antenna sensor; (b) change in the distance $d$ due to pressure; (c) effect of pressure on the loop antenna frequency .....	61
4.7	Capacitance of the circular loop antenna versus distance from reflector $d/\lambda$ .....	63

4.8	Experimental setup for pressure measurement .....	64
4.9	Effect of pressure on the resonant frequency of the loop antenna sensor; (a) resonant frequency at various pressure values; (b) resonant frequency shift (GHz) vs. pressure (psi); (c) effect of hysteresis on the loop antenna sensor .....	65
4.10	Hybrid integration of shear/pressure sensor (not to scale): (a) side view; (b) top view .....	66
4.11	Fabricated smart shoe prototype .....	67
4.12	Schematic of sensor interrogation principle .....	68
4.13	Change in power output due to pressure applied on the sensor.....	69

## CHAPTER 1

### INTRODUCTION

The maintenance and repair of mechanical and aerospace systems involve vast amounts of resources in terms of manual labor, materials and finance. Increasingly, in view of the extensive investment required to fabricate new systems, existing systems are frequently re-commissioned so that they can remain in service beyond their planned operational life (Ko and Ni 2005, Chang *et al* 2003). However, it is imperative that proper attentions are given to ensure their safe operation under various loading conditions (Giurgiutiu and Cuc 2005). Hence it is vital to incorporate appropriate Structural Health Monitoring (SHM) mechanisms into these systems. The process of embedding damage detection and characterization systems on engineering structures is called Structural Health Monitoring (SHM). Here damage is defined as the material and/or geometrical property changes of a structure which adversely affect the system's performance. SHM is basically a three step process; observation of a system over time using an array of sensors, extraction of damage-sensitive features from sensor measurements and analysis of these features to determine the current state of system health. SHM employs smart sensors that are capable of measuring the damage directly or sensing indirect parameters such as strain, temperature, humidity etc. These sensing systems can continuously monitor the health state of structures and could provide an alert when the damage is critical and needs human intervention. Currently, SHM is

emerging as an important component in maintaining structural integrity of spacecraft components, bridges and aircrafts. In addition to the Army and Air Force, other federal agencies such as the Federal Aviation Administration, NASA and Department of Transportation are also interested on SHM (Yolken 2005, Butterworth-Hayes 2003, Talbot 2003). Many SHM techniques have already been deployed and proven to be quite efficient. The techniques are being considered for implementation on almost every new major air and spacecraft from the Lockheed Martin F-35 to the Boeing 7E7 to reusable space vehicles. However, the near term challenge is to develop a robust system, which is capable of operating in most environmental conditions with long term reliability. SHM provides several unique advantages such as better estimation on current health state of a structure, potential eradication of catastrophic failures, and reduced downtime and maintenance costs as compared to traditional nondestructive inspections (Bakht *et al* 2001).

## 1.1 Crack Detection Sensor

### *1.1.1 Importance of crack detection*

One of the major tasks of SHM systems is crack detection and monitoring in load-bearing structures. Majority of cracks are generated due to fatigue loadings. Despite the fact that engineering components and structures are carefully designed against fatigue failures, 50 to 90% of mechanical failures are due to fatigue crack development (Foong *et al* 2006). Fatigue damage, in the form of cracks, occurs in structures subjected to cyclic loading. In most cases, components containing fatigue cracks can operate safely until the crack reaches a critical crack length. This duration

not only depends on the physical length of the crack but also depends on the relative orientation between the crack and the loading direction. Moreover, in most crack detection/monitoring cases, the crack detection sensor is pre-installed on the structure before the crack emerges. Even though past experience and/or stress analysis may help us estimate where the crack might emerge and how it might propagate, the actual crack propagation might deviate from the anticipated direction. Therefore, a crack detection sensor that is sensitive to both the crack length and its orientation is needed.

#### *1.1.2 Existing crack detection techniques*

A large number of SHM sensor techniques have been employed to detect crack propagation in metallic structures. One of the most popular crack detection schemes is the ultrasound based non-destructive evaluation technique (Shan and Dewhurst 1993, Giurgiutiu and Bao 2002, Chang and Ihn 2004, Shin and Rose 1998). By studying the interactions between a propagating ultrasonic wave and the crack, crack detection over a relatively large area using a few ultrasonic actuators/sensors was achieved. In addition, the ultrasonic waves generated by crack propagation, *i.e.* the acoustic emission (AE) signals, were also analyzed for crack detection and localization (Hamstad *et al* 2002). Extracting quantified crack information and separating crack effects from other interference sources (temperature fluctuations, reflections from structure discontinuities, and noises, *etc.*) are two biggest challenges of using ultrasound-based mechanisms for crack detection (Yu and Giurgiutiu 2005, Chen *et al* 1999, Volkovas *et al* 2006, Shigeishi *et al* 2001, Rizzo *et al* 2009). Point-wise strain sensing was employed to provide better quantified crack information than ultrasound-based techniques (Liu *et al*

2007, Murphy *et al* 1997). However, strain-based crack detection requires placing the sensors close to the crack. Without knowing the crack location in advance, a large number of sensors are required. Electromagnetic waves, such as Eddy current (Sadler and Ahn 2001, Smith and Hugo 2001), Electromagnetic emissions (EME) (Koktavy 2009, Sedlak *et al* 2008) and ground penetrating radars (Huston *et al* 2000), were also exploited for crack detection. Most of these crack detection systems need high power, are bulky, or do not have sufficient resolution to determine the exact location and dimension of the cracks.

Very few sensor techniques are reported in the literature which can detect crack orientation. Most of the reported crack orientation detection techniques are based on ultrasound reflection and scattering. Chang and Mal (1999) investigated the crack orientation detection by evaluating the time and frequency spectra of lamb waves scattering around a circular hole with edge cracks. However, quantitative analysis of the crack orientation was not discussed. Lu *et al* (2007) quantitatively analyzed the crack orientation using multiple sets of ultrasound transducers. Each set has one actuator and two sensors; one sensor measures the reflection whereas the other measures the transmission. In this case, signal processing of cracks oriented parallel to the incident waves was a difficult task owing to the possibility of the reflected wave overlapping with the incipient wave. Other techniques to quantitatively detect crack orientation include analyzing the directionality pattern (Kinra and Vu 1986) and studying the amplitudes of Hilbert spectra of the reflected lamb waves (Ni *et al* 2010). Again, multiple sets of ultrasound transducers are needed for orientation quantification.

Nonetheless, blind zones existed for both techniques. A few researchers also attempted to analyze the crack orientation based on the time-of-flight of laser-generated Rayleigh waves (Matsuda *et al* 2006). However, the crack location has to be known *a-priori* to effectively detect the crack orientation.

It can be concluded that most common technical challenges in crack detection sensors are size, cost, resolution, sensitivity, power required to operate the sensor and most importantly, the ability to detect both crack propagation and crack orientation. Given the serious consequences of cracks propagating at an angle to the loading direction, research in this area is absolutely vital. Considering that the ultimate goal of SHM systems is to provide sensory information to facilitate decision making regarding the remaining useful life of the service components, a new type of sensor that can detect cracks and provide quantified crack growth as well as orientation information is needed.

### *1.1.3 Proposed crack detection sensor*

The proposed crack detection sensor is based on a microstrip patch antenna. The resonant frequencies of a dual-frequency patch antenna are sensitive to the crack propagation in the ground plane of the sensor. Based on this principle, crack propagation and crack orientation can be monitored from the resonant frequency shifts of the antenna sensor. The patch antenna's capability to monitor crack was validated using fatigue testing of a compact tension specimen. The detailed specimen preparation, the sensor fabrication, and the experimental procedure are presented in chapter 3. The experimental results demonstrated that the antenna sensor can monitor crack propagation with sub-millimeter resolution.

## 1.2 Shear/compression Sensor

Diabetic foot complications such as foot ulcers are the most common cause of nontraumatic lower extremity amputations. It is also the most frequent reason for hospitalization of patients with diabetes. Ulcer formation is believed to be contributed by mechanical stresses acting on the foot (Garrow *et al*, Hosein and Lord, Davis *et al*). Mechanical stresses acting on a healthy foot during regular walking do not cause any serious tissue damage. However, in cases of foot pathology such as diabetic foot, these stresses might cause severe damages. This might be due to the change in the stress distribution or the decreased tolerance to stress. Without proper care, ulceration can lead to infection and amputation. As a matter of fact, foot ulcer is the initiating factor in 85% of all diabetic amputations (Apleqvist and Larsson 2000). Therefore, monitoring stress distribution on the foot is very important to understand and diagnose foot ulcers. Over the past few decades, the importance of monitoring forces on the foot for the prediction of ulceration has been emphasized by several researchers (Veves *et al* 1992, Duckworth *et al* 1985, Wu *et al* 2007). The forces acting at the foot-insole interface were classified into two components, i.e., pressure and shear (Hosein and Lord 2000). The pressure on the foot is the vertical normal force due to human weight whereas the shear forces are the lateral horizontal forces exerted on the foot during ambulation. Measuring both shear and pressure is critical for evaluating the stresses acting on the foot. Several studies have found that careful inspection of the diabetic foot on a regular basis is one of the easiest, least expensive and most effective measures for preventing

foot ulcers (Wylie-Rossett *et al*, Bailey *et al*). This continuous real-time inspection of foot can only be accomplished with in-shoe sensors.

### *1.2.1 Existing pressure detection sensors*

Many researchers tried to accomplish the task of measuring the plantar pressure distribution. Hughes *et al* utilized an interferometry technique that involves the use of a laser light directed onto a pressure sensitive plate. The pressure plate compresses when a load is applied, which in turn is monitored by the interferometry technique. The interference pattern gives the pressure distribution across the plate. However, this technique has a low spatial resolution. Wang *et al* utilized dual arrays of optical fibers oriented perpendicular to one another and separated by elastomeric pads, which could be used inside a shoe. The reduction in light output indicates the magnitude of pressure applied over the sensor. But the authors had problems with consistent and accurate placement of sensors inside the shoe. In addition, cost and noise was also high due to the use of many optical components. Many other in-shoe sensors were proposed to evaluate plantar pressure (Tao *et al* 2009, Brandes *et al* 2007, Lee and Park 2008, Munk-stander 2006, Kong and Tomizuka 2009, Hirasawa *et al* 2007, Titianova *et al* 2004). The pressure monitoring sensors such as capacitance mats (Abraham *et al* 2011) and piezoelectric multi-element plates (Nevill *et al* 1995, Geng *et al* 2010, Abhinav 2006) offered good spatial definition and resolution. However, the resolution of these sensors was poor. Based on the pressure distribution obtained from various pressure sensors, it was proved that high pressures under the foot led to ulcer formation (Murray *et al* 1996, Boulton *et al* 1983, Ctercteko *et al* 1981). A clear relationship was

established between areas of high plantar pressure and ulceration (Laborde 2010, Brike et al 1995).

### *1.2.2 Existing shear detection sensors*

The in-shoe shear measurement has not been used clinically for diabetic foot diagnosis yet, mainly due to the lack of miniature shear sensing transducers (Lebar *et al* 1993).

There are very few sensors reported in the literature which can measure shear forces on the foot. The very first sensor to detect shear-force was based on the magneto-restrictive principle, where the transducer was constructed using two stainless steel discs (16 mm diameter and 2.7 mm thick), with magnet fixed to one of the discs and magneto-resistor fixed to the other (Tappin *et al* 1980). The two discs are cemented together with a silicon rubber and any lateral movement (shear deformation) of the magnet produces an electrical signal proportional to the movement of the magnet. Shear sensor designs based on a copolymer film were produced subsequently for improved flexibility (Akhlaghi and Pepper 1996). The copolymer film sensors were easy to fabricate and could detect shear under the foot with a reasonable sensitivity. However, they required a lot of data processing and the data acquisition system is complex (Akhlaghi 1995). Another group of researchers proposed a circular shear transducer consisting of two circular discs and two flat springs. The response time of these sensors was very fast, but the sensors suffered with low operating range and high hysteresis loss. In contrary, the shear sensors based on micro-electro mechanical systems (MEMS) have a high sensitivity, high resolution and low hysteresis. But the MEMS sensors were prone to electromagnetic interferences (Missinne *et al* 2010). The

problems associated with the electromagnetic interferences were overcome with optical fiber shear sensors (Wang *et al* 2005). The optical fiber sensors were conformal and flexible, making them a good choice for in-shoe sensors. However, they are fragile and prone to damage during regular use. Therefore, an extensive research strategy which can measure the plantar shear with high sensitivity, resolution, robustness, and with a minimum hysteresis is required. In addition, one of the biggest limitations of all the published pressure and shear sensors is their wire connection, which making embedding them in shoes cumbersome. Not only do the wire connections limit the range of motion, they also cause long-term durability concerns if the instrumented shoes will be worn by the patient on a regular basis.

### *1.2.3 Proposed shear sensor*

The proposed shear detection patch antenna sensor is very similar to the crack detection sensor. The shear detection sensor, i.e., a microstrip patch antenna, consists of a dielectric substrate with a ground plane on one side and an antenna patch on the other side of the substrate. A slot is introduced in the ground plane of the antenna sensor and any shear force applied on the patch causes the substrate to deform laterally. This essentially increases the overlapping length between the slot and the patch, resulting in a frequency shift of the antenna. Similarly, the shear acting perpendicular to the width of the antenna patch can be evaluated by adding a slot perpendicular to the length direction of the patch and monitoring the corresponding frequency of the antenna sensor. Therefore, bi-directional shear forces acting on the foot can be measured using a patch antenna sensor.

#### *1.2.4 Proposed pressure sensor*

The antenna sensor used for pressure detection is similar to a microstrip loop antenna. It consists of three components: a flexible sheet of dielectric substrate, a loop printed on one side of the substrate, and a ground plane coated on the other side of the dielectric substrate. Here, the pressure applied on the loop antenna sensor changes the distance between the ground plane and the loop antenna sensor. This causes a change in the resonant frequency of the loop and thus the pressure can be quantitatively measured from the frequency shift.

### 1.3 Advantages of the Proposed Sensor

The advantages of the antenna sensor over conventional sensors are summarized as the following:

- High resolution: Patch antenna sensors have a very high resolution when compared to many conventional sensors
- Wireless interrogation: The patch antenna sensors can be wirelessly interrogated from a distance (Deshmukh *et al* 2010)
- Multiplexing capability: The patch antenna sensors can be multiplexed to form a wireless sensing network that can provide sensor coverage over a large area (Xu and Huang 2011).
- The sensor also has a low profile, light weight, low fabrication cost.

### 1.4 Thesis Indexing

Chapter 1 gives an introduction to SHM and an overview of the antenna sensors used to detect crack propagation, crack orientation, and shear/compression. Chapter 2

discusses the microstrip antenna theory and the modeling of the antenna sensor using transmission line model. The design of the antenna sensor is also discussed. Chapter 3 deals with crack length and orientation detection using the patch antenna sensor, whereas chapter 4 discusses the application of antenna sensors for shear/compression sensing. Concluding remarks are given in chapter 5 and finally Chapter 6 deals with the future work.

## CHAPTER 2

### MICROSTRIP ANTENNA DESIGN

This chapter introduces the fundamental working principle of a rectangular microstrip patch antenna and the transmission line model of the patch antenna.

#### 2.1 Introduction

Microstrip patch antennas (also known as patch antennas) are among the most common antenna types in use today, particularly popular in the frequency range of 1 to 6 GHz. The first intense development of patch antennas occurred in 1970's. The flat profile, thin structure and reduced weight, compared to parabolic reflectors and other antenna options, made it attractive for airborne and spacecraft applications. Most recently, all the patch antenna properties, with additional size reduction using high dielectric constant substrates, have made patch antennas common in hand-sets, GPS receivers and other mass-produced wireless products. There are many variations in a patch antenna design, but the basic configuration is shown in figure 2.1(a). A patch antenna is a layered structure with two parallel conductors separated by a dielectric substrate. The dielectric substrate is usually made of a thin sheet of low-loss insulating material. The antenna patch is on one side of substrate and a metal conductor on the other side acts as a ground plane. The metallic patch and the ground plane form an electro-magnetic (EM) cavity so that a resonance can be generated and the fringing field between the ground plane and the patch can efficiently radiate. The two edges of the

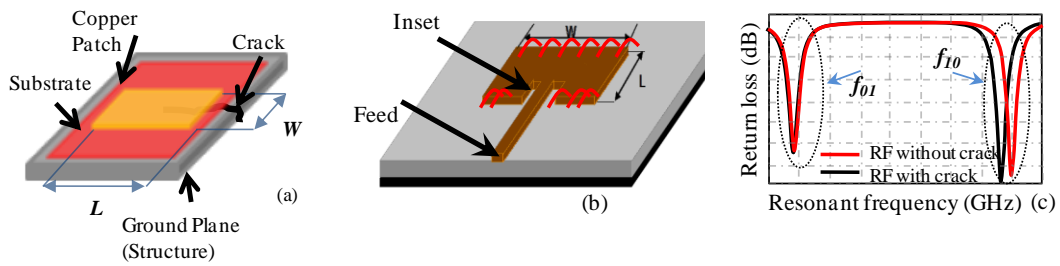


Figure 2.1: Schematic of microstrip patch antenna; (a) patch antenna; (b) current directions in the patch; (c)  $S_{11}$  parameters of a patch antenna

patch that are connected to the feed connection provide the radiation, acting as slot antennas, where each slot is the gap between the edge of the patch and the ground plane beneath the intervening dielectric layer. The arrows at the left and right edges of the patch represent the currents between the patch conductor and the ground plane (see figure 2.1 (b)). At the edges, where they are not contained, these currents result in the desired radiation of electromagnetic waves from the two edge slots.

The radiation behavior of the antenna can be described by the scattering parameters, or S-parameters. The S-parameters describe the signals radiated or reflected by the patch antenna. In the context of the S-parameters, scattering refers to the way in which the travelling currents and voltages in a transmission line are affected when they meet a discontinuity caused by the insertion of a network into the transmission line. S-parameters are useful in microwave design because they are easier to measure and to work-with at high frequencies, conceptually simple and provide a detailed insight into a measurement and modeling problem. An electrical network to be described by the S-parameters may have any number of ports. Ports are

the points at which electrical signals either enter or exit the network. The S-parameters can be easily understood by comparing them with a pair of spectacles (see figure 2.2(a)). When an incident reference wave is transmitted through a spectacle glass, part of the reference wave is transmitted through the glasses and the remaining is reflected back. The signal flow graph shown in figure 2.2(b) clearly illustrates the S-parameter interpretation. For a two-port system, the S-parameters can be defined as:

$$\begin{bmatrix} b_1 \\ b_2 \end{bmatrix} = \begin{bmatrix} S_{11} & S_{12} \\ S_{21} & S_{22} \end{bmatrix} = \begin{bmatrix} a_1 \\ a_2 \end{bmatrix} \quad (2.1)$$

where  $a_1$ ,  $a_2$  are the power wave travelling towards the two ports and  $b_1$ ,  $b_2$  are the power waves reflected from the two ports. There are four S-parameters, denoted as  $S_{11}$  (reflection coefficient at port 1),  $S_{21}$  (transmission coefficient from port 1 to port 2),  $S_{12}$  (transmission coefficient from port 2 to port 1) and finally  $S_{22}$  (reflection coefficient at port 2). Each parameter is typically characterized by a magnitude in decibels and a phase in radians. For a one-port device such as a patch antenna, there is only one S-parameter, *i.e.*,  $S_{11}$ . A typical  $S_{11}$  curve of a patch antenna is shown in figure 2.1 (c). The return loss is a parameter which indicates the amount of power that is “lost to the

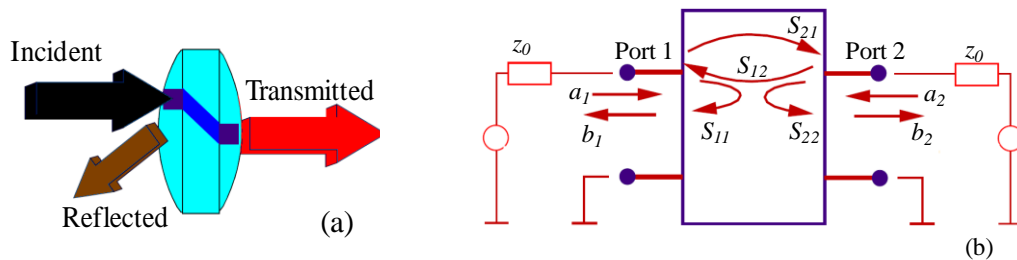


Figure 2.2: S-parameter illustration; (a) power reflected at spectacles; (b) two port network

load” and does not return to the measurement port. The return loss is the largest at the resonant frequency of the patch antenna, resulting in a dip at the resonant frequency in the  $S_{11}$  curve.

## 2.2 Antenna Modeling

There are many different analytical models for a microstrip patch antenna. The most popular are the transmission line model (Carver and Mink 1981), cavity model (Lo *et al* 1979) and full-wave model (Rana and Alexopolous 1981). The transmission line model is the simplest of all and also gives a good physical insight into the patch antenna.

The transmission line model represents the microstrip antenna by two slots, separated by a low-impedance transmission line. Because the dimensions of the patch are finite along the length and width direction, the fields at the edges of the patch undergo fringing (Balanis 2005). The amount of fringing is dependent on the patch dimensions and the height of the substrate. Ideally, fringing is a function of the ratio of

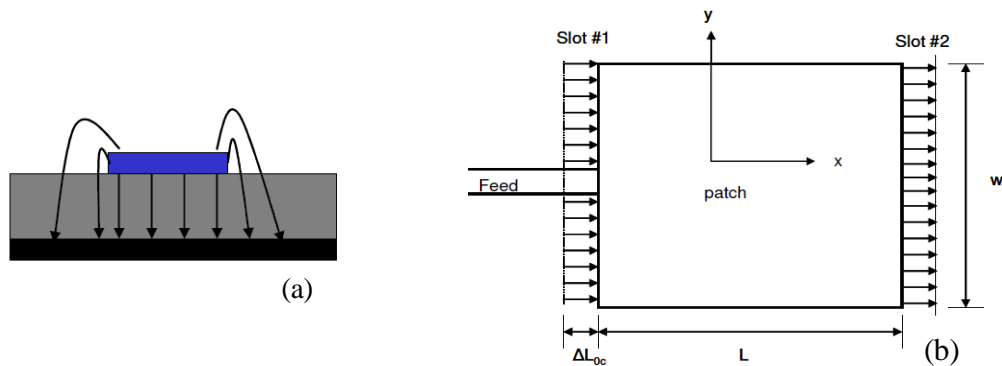


Figure 2.3: (a) Electric field lines on a patch antenna (side view); (b) top view showing tangential fringing electric fields that are responsible for radiation.

the patch length and the substrate height ( $L/h$ ) as well as the dielectric constant of the substrate  $\epsilon_r$ . Typical electric fields for a patch antenna are shown in figure 2.3(a). It is evident that most of the electric field lines exist in the substrate and some of the field lines are in the air. Since some of the waves travel in the substrate and some in air, an effective dielectric constant  $\epsilon_{re}$  is introduced to account for the fringing and the wave propagation. For a patch surrounded by air, the effective dielectric constant will have a value somewhere between the dielectric constant of air (dielectric constant of air = 1) and the substrate dielectric constant  $\epsilon_r$ . For most applications where the dielectric constant of the substrate is greater than unity, the effective dielectric constant will be closer to the dielectric constant of the substrate. The effective dielectric constant is calculated from the dielectric constant  $\epsilon_r$ , the thickness  $h$  of the substrate and the electric width of the patch  $w_e$ , *i.e.*

$$\epsilon_{re} = \frac{\epsilon_r + 1}{2} + \frac{\epsilon_r - 1}{2\sqrt{(1 + 10h/w_e)}}. \quad (2.1)$$

At a specific radiation frequency  $f$ , the electric width of the patch antenna sensor is calculated from the free-space velocity of light  $c$ , permittivity  $\epsilon_0$ , permeability  $\mu_0$  and dielectric constant of the substrate  $\epsilon_r$  as

$$w_e = \frac{1}{2f\sqrt{\mu_0\epsilon_0}} \sqrt{\frac{2}{\epsilon_r + 1}}, \quad (2.2)$$

The fringing electric fields cause the patch antenna to look larger than its physical dimensions (see figure 2.3(b)). The dimensions on each end of the patch antenna have been extended by a distance  $\Delta L_{oc}$ , which is a function of the effective dielectric constant

and the width-to-height ratio ( $w/h$ ). This extension is also related to the effective dielectric constant  $\epsilon_{re}$ , the substrate thickness  $h$  and the electric width  $w_e$  as

$$\Delta L_{oc} = 0.412h \frac{(\epsilon_{re} + 0.3)(w_e / h + 0.264)}{(\epsilon_{re} - 0.258)(w_e / h + 0.813)}. \quad (2.3)$$

Since the patch has been extended on both sides by  $\Delta L_{oc}$ , the effective length of the patch is given as

$$L_e = L + 2\Delta L_{oc}, \quad (2.4)$$

where  $L$  is the geometric dimension of the patch along the direction of the radiation current. For antenna design, the length of the patch antenna can then be calculated from the above equation for a selected radiation frequency of  $f$  as

$$L = \frac{c}{2f\sqrt{\epsilon_{re}}} - 2\Delta L_{oc}. \quad (2.5)$$

A patch antenna with a rectangular antenna patch can radiate at two fundamental radiation modes,  $TM_{10}$  and  $TM_{01}$ , with the current of the  $TM_{10}$  flowing along the length direction and the  $TM_{01}$  current flowing along the width direction. The corresponding radiation frequencies for these two radiation modes are therefore termed  $f_{10}$  and  $f_{01}$  respectively. The length and width of the antenna patch can then be calculated from equation (2.5) and (2.2) once these two radiation frequencies are selected.

In order to excite the two radiation modes simultaneously, a microstrip transmission line, usually with an impedance of  $50 \Omega$  can be connected to the antenna patch. To match the impedances of the microstrip transmission line and the antenna patch at both resonant frequencies, the transmission line and the antenna patch have to

be connected at a proper position (Chen and Wong 1996). This optimum feeding position was determined based on the impedance matching (Balanis 2005), i.e.,

$$x_0 = \frac{L}{\pi} \cos^{-1} \left( \sqrt{\frac{50}{R_{iny}}} \right), \quad (2.6)$$

$$y_0 = \frac{w}{\pi} \cos^{-1} \left( \sqrt{\frac{50}{R_{inx}}} \right), \quad (2.7)$$

where  $x_0$  and  $y_0$  represent the distance from the  $X$  and  $Y$  axes respectively. The calculation of the resonant input resistances,  $R_{inx}$  and  $R_{iny}$ , is given by Balanis (2005).

## CHAPTER 3

### CRACK DETECTION USING PATCH ANTENNA

This chapter discusses the principle of operation of using the patch antenna for crack detection. It also includes the experiment methodology, experimental results and the correlation of the antenna frequency shift to the crack propagation length. In addition to crack propagation, the ability of the patch antenna sensor to detect crack orientation and hidden cracks is also discussed. It was demonstrated that the patch antenna sensor can detect cracks with sub-millimeter resolution and can also detect various crack orientations using a single frequency parameter  $R$ . In addition to the surface crack propagation, a wireless interrogation technique to detect hidden cracks is also presented.

#### 3.1 Proposed Crack Detection Sensor

The proposed crack detection sensor has identical configuration as microstrip patch antennas, i.e. it consists of a dielectric substrate with a ground plane on one side of the substrate and an antenna patch printed on the other side of the substrate (see figure 3.1(a)). For an antenna sensor with a perfect ground plane, the resonant frequencies ( $f_{10}$  and  $f_{01}$ ) of these resonant modes ( $TM_{10}$  and  $TM_{01}$ ) are related to the corresponding electric field dimension as

$$f = \frac{c}{2\sqrt{\epsilon_e} L_e + 2\Delta L_c}, \quad (3.1)$$

where  $c$  is the velocity of light in vacuum,  $\epsilon_e$  is the effective dielectric constant of the

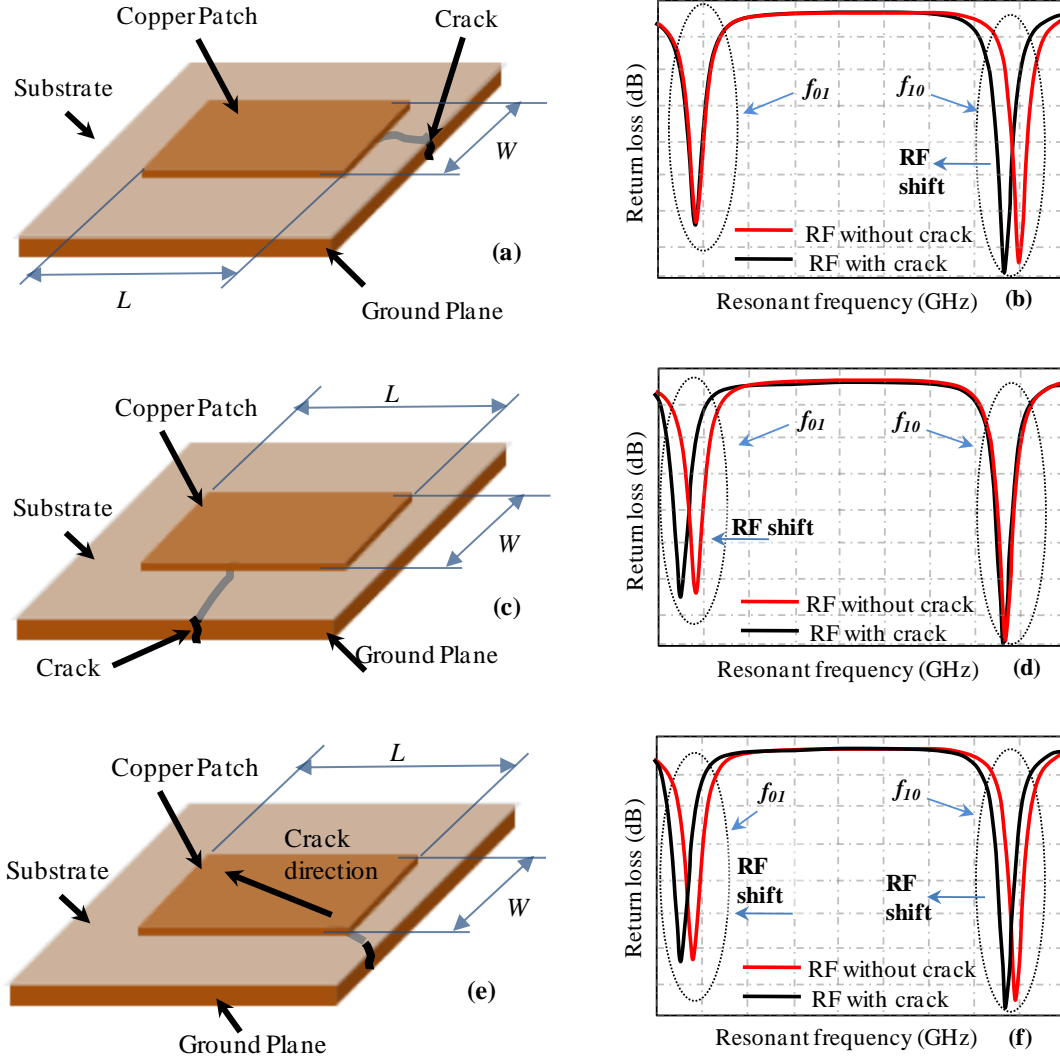


Figure 3.1: Principle of antenna sensor for crack detection; (a) & (b) antenna sensor with a crack along its length and its effect on the  $f_{10}$  frequency; (c) & (d) antenna sensor with a crack along its width and its effect on the  $f_{01}$  frequency; (e) & (f) antenna sensor with an inclined crack and its effect on both  $f_{10}$  and  $f_{01}$  frequencies.

substrate, and  $\Delta L_c$  is the line extension.  $L_e$  is the electric length of the radiation mode (Balanis 2005), which is the geometrical dimension of the antenna patch that is parallel to the respective electric current direction. Therefore, a rectangular antenna patch having a larger dimension along its length direction will have a lower  $TM_{01}$  resonant frequency  $f_{01}$  and a higher  $TM_{10}$  resonant frequency  $f_{10}$ . The conductivity of the ground plane also affects the resonant frequencies. When a crack is introduced along the length direction of the antenna patch, it partially cuts off the current flow along the width direction and forces the current to flow around the crack. As a result, the current path along the width direction is increased, essentially increasing the electrical length of the  $TM_{10}$  mode. Since the resonant frequency is inversely proportional to the electrical length, the resonant frequency  $f_{10}$  reduces with the crack propagation (see figure 3.1(b)). The amount of reduction in the  $f_{10}$  frequency is determined by the overlapping length between the crack and the antenna patch, i.e., the crack length underneath the antenna patch. On the other hand, the  $TM_{01}$  current flow is not disturbed by the crack since the crack is parallel to its current flow. Therefore, the resonant frequency  $f_{01}$  remains the same as if there is no crack presence. A crack that is parallel to the width direction of the patch will have exactly the opposite effect on the  $f_{01}$  and  $f_{10}$  frequencies as compared to a crack that is parallel to the length direction of the antenna patch, as shown in figure 3.1(c) and 3.1(d). If an inclined crack is introduced, the current flow along both the directions of the patch is distorted (see figure 3.1(e)). As a result, both resonant frequencies will shift towards lower frequencies (see figure 3.1(f)). Since different crack orientations change the resonant frequencies of the antenna sensor in a different

way, the crack orientations can be identified from the resonant frequency shifts of the antenna sensor.

### *3.1.1 Design of compact tension specimen*

In order to evaluate the feasibility of the patch antenna to detect crack propagation, a special compact tension (CT) specimen was designed to control the crack propagation. A compact tension (CT) specimen is a standard single edge-notch specimen in accordance with the ASTM and ISO standards. The geometry of the standard CT specimen is given in ASTM standards E647 and is also shown in figure 3.2 for readers' convenience. Since the stresses are the highest at the notch, a crack initiates at the notch and propagates at a direction that is parallel to the notch direction when cyclic tensile loading is applied on the specimen. As a common practice, CT specimen is used in fracture mechanics and corrosion testing to establish the fracture toughness of a given material.

### *3.1.2 Design of CT specimen and sensor preparation*

To characterize the antenna sensor's performance for crack monitoring, the antenna sensor was bonded to a pre-cracked Compact Tension (CT) specimen made of Aluminum alloy 7075-T6. The CT specimen was designed and machined per ASTM standard E647-00. After machining, the CT specimen was polished using 400, 600 and 1500 grit sand papers to smoothen the surface. The polished CT specimen was subjected to a 5 Hz cyclic loading to introduce a 0.125 inch pre-crack.

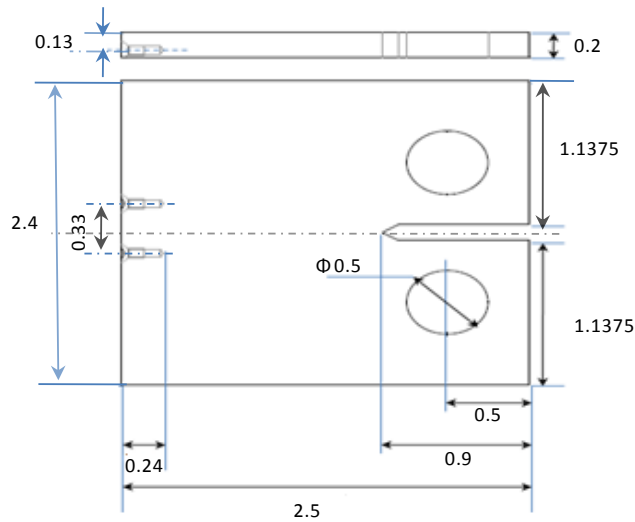


Figure 3.2: Design of CT specimen.

The antenna sensor and the CT specimen assembly was prepared by directly bonding a rectangular dielectric substrate (Kapton FN, 50  $\mu\text{m}$  in thickness, 2 in. x 1.5 in.) on the pre-crack specimen using superglue. To ensure a good bonding, the surfaces of the Kapton film were slightly sanded. A 66  $\mu\text{m}$  thick copper strip (3M 118, 0.6 inches long and 0.5 inches wide) was then bonded on top of the Kapton film. The copper strip was oriented in such a way that the pre-crack was aligned with the center line of its width direction and the crack tip was at a distance of 0.1 inch away from the patch. Since the CT specimen itself is conductive, it also serves as the ground plane for the antenna sensor. This construction resulted in a highly flexible, low cost, robust, and conformal antenna sensor. The antenna sensor can be excited contactly using a microstrip feed line or non-contactly using a horn antenna (Deshmukh et al 2010). Since this study is focused on understanding the effects of the crack on the resonant frequencies of the antenna sensor, we used the microstrip feeding method. A 1 mm wide

microstrip feed line, made of the same copper film, was bonded next to the antenna patch. Conductive epoxy was dabbed on the patch/feed-line interface to improve the electric connection between the patch and the feed line. To facilitate connecting an SMA connector to the feed line, the CT specimen was designed with two screw holes at the edge. After fabricating the patch antenna, the SMA connector was mounted on the CT specimen with its pin touching the end of the microstrip feed line. Figure 3.3(a) shows the antenna sensor/SMA connector assembly. The location of the antenna sensor was marked on the opposite side of the CT specimen. To facilitate measuring the crack length using a digital camera, reference marks with a separation of 2 mm were also drawn on the specimen. A digital image of the CT specimen with the antenna patch position and the reference marks is shown in figure 3.3(b). Based on the ASTM standard E647-00, the crack growth rate for a CT specimen has to be greater than a threshold value of  $10^{-8}$  m/cycle and the load ratio  $R = P_{max}/P_{min}$  can be taken anywhere between 0 and 1. Curve fitting the experimental data provided in (Skinn et al 1994), we found the relationship between the crack growth rate ( $da/dN$ ) and stress intensity factor range ( $\Delta K$ ) for Al 7075-T6 is

$$\log(da/dN) = 0.58 \log(\Delta K) - 8.5012 \quad (3.2)$$

Assuming the precrack is 0.125 inch in length,  $\Delta K$  should be 40661 psi-in<sup>1/2</sup> for a crack growth rate of  $10^{-8}$  m/cycle. The stress intensity factor of a CT specimen subjected to an external P is given by (Grandt 2003)

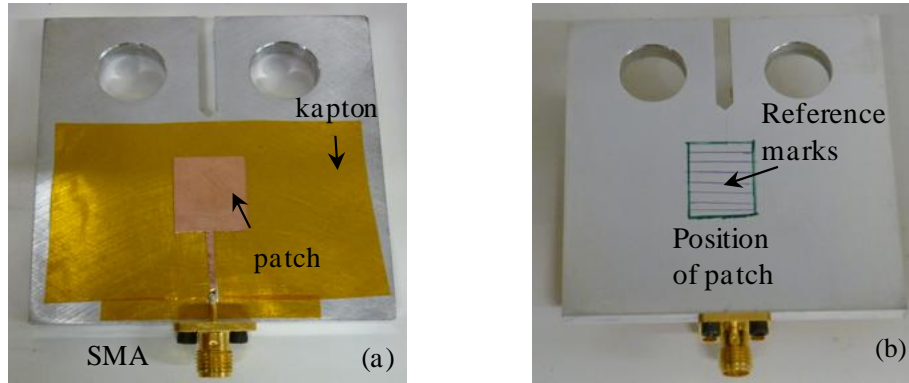


Figure 3.3: (a) antenna sensor/SMA assembly; (b) reference marks on the back side of the specimen.

$$K = \frac{P}{B\sqrt{W}} \left[ \frac{(2+\alpha)}{(1-\alpha^{1.5})} \left( 0.886 + 4.64\alpha - 13.32\alpha^2 + 14.72\alpha^3 - 5.6\alpha^4 \right) \right] \quad (3.3)$$

where  $W$  is the specimen width,  $B$  is the specimen thickness, and  $\alpha$  is the ratio between the crack length  $a$  and  $W$ . Selecting a load ratio  $R = 0.5$ , the maximum and minimum loads are calculated from the selected  $\Delta K$  to be 620 lbs and 310 lbs. Since the stress intensity factor increases with the crack length  $a$ , the crack growth rate will always be greater than the required threshold value as the crack length increases.

### 3.1.3 Experimental setup

The experimental setup to propagate the crack using fatigue cycling is shown in figure 3.4. The CT specimen was subjected to a fatigue loading (5 Hz loading frequency,  $P_{max} = 620$  lb, and  $R = 0.5$ ) using a close-loop servo-hydraulic MTS machine. During the fatigue test, a Vector Network Analyzer (VNA) (Rohde & Schwarz, ZVA 24) was connected to the antenna sensor via the SMA connector and the  $S_{11}$  curves of the antenna sensor at different crack lengths were measured. The VNA was programmed to acquire the  $S_{11}$  curves from 5 GHz to 10 GHz with a frequency

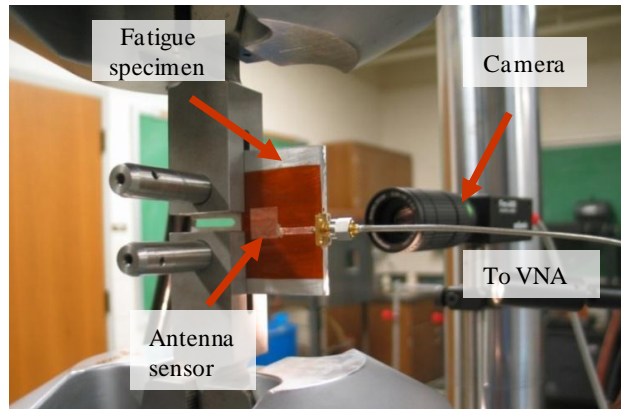


Figure 3.4: Experimental setup for fatigue testing.

resolution of 1.25 MHz (4000 data points over 5 GHz). A CCD camera was placed facing the opposite side of the antenna sensor. The digital images were acquired by a computer and displayed on a monitor. Whenever the crack reached a reference mark, the test was paused and the  $S_{11}$  curves of the antenna sensor under different loads were recorded. After taking the measurements, the test was resumed until the crack reached the next reference mark and the measurements were repeated. The experiment was terminated when the crack spanned the entire length of the antenna patch.

#### 3.1.4 Experimental results and analysis

The  $S_{11}$  curves of the antenna sensor around the  $f_{10}$  frequency at different crack tip locations are shown in figure 3.5(a). The rightmost curve, was measured when the crack tip was exactly under the left edge of the antenna patch, which means there was no overlap between the crack and the antenna patch. Each subsequent shift of the curve set to the left corresponds to a crack propagation of 1 mm. The leftmost curve (i.e., the red curve) represents the  $S_{11}$  curves when the crack tip has propagated 6 mm under the

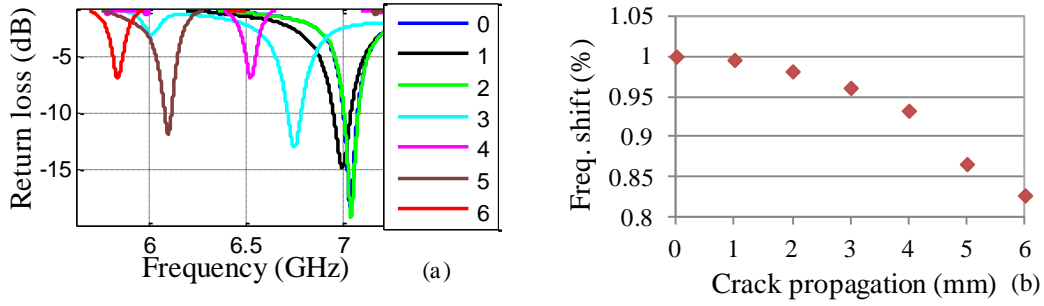


Figure 3.5: Effect of crack growth on  $f_{10}$  frequency; (a) shift of the  $S_{11}$  curves with crack growth; (b)  $f_{10}$  frequency vs. crack tip locations.

antenna sensor. The  $f_{10}$  frequencies of the antenna sensor as identified from the  $S_{11}$  curves are plotted versus the crack tip locations in figure 3.5(b). The tip locations were measured from the left edge of the antenna patch, *i.e.* the tip location values are also the overlapping length between the antenna patch and the crack. As expected, the  $f_{10}$  frequency shifted towards the lower frequencies when the crack length increased. We observed a non-linear relationship between the  $f_{10}$  frequency and the crack length. Regardless, sub-millimeter crack growth can be detected from the antenna frequency shift as long as the relationship between the crack length and the antenna frequency is established. It is worth noting that the antenna patch was torn when the crack propagated half-way into the antenna patch. As a result, the antenna frequency was no longer measurable for crack propagations more than 6 mm. In section 3.2, a technique that improves the reliability of the antenna sensor was described.

To evaluate the effect of crack growth on the  $f_{01}$  frequency, *i.e.* the antenna frequencies along the length direction, the  $S_{11}$  curves of the antenna sensor as well as its  $f_{01}$  frequencies at various crack tip positions are plotted in figure 3.6(a) and 3.6(b).

Unlike the  $f_{10}$  frequency that decreased with the crack growth, the  $f_{01}$  frequency increased with the crack growth. The relationship between the  $f_{01}$  frequency and the crack tip locations are not linear as well. There is a considerable increase on the  $f_{01}$  frequency when the crack tip crossed the left and right edge of the antenna patch while the  $f_{01}$  frequency remained relatively constant when the crack was propagating underneath the antenna patch. This phenomenon can be explained by the current density pattern of the  $TM_{01}$  radiation mode as shown in figure 3.6(c) (Horng *et al* 1994). For the  $TM_{01}$  radiation mode, the current density is much higher at either edge of the patch and is constant in the interior of the antenna patch. The high current density regions appear to be corresponding to the high crack sensitivity of the  $f_{01}$  frequency. Because the effects of the crack on the  $f_{01}$  and  $f_{10}$  frequencies are entirely different, we would be able to determine the orientation of the crack even if the crack orientation were not known in advance. In addition, the  $f_{01}$  frequency also gives a strong indication on when the crack tip reaches the antenna patch and when it propagates through the antenna patch. The sudden increases in  $f_{01}$  frequency could serve as references to determine the exact location of the crack tip. In some cases, the crack may change its direction after it is below the patch. This sudden increase in  $f_{01}$  frequency can also indicate if the direction of the crack changes.

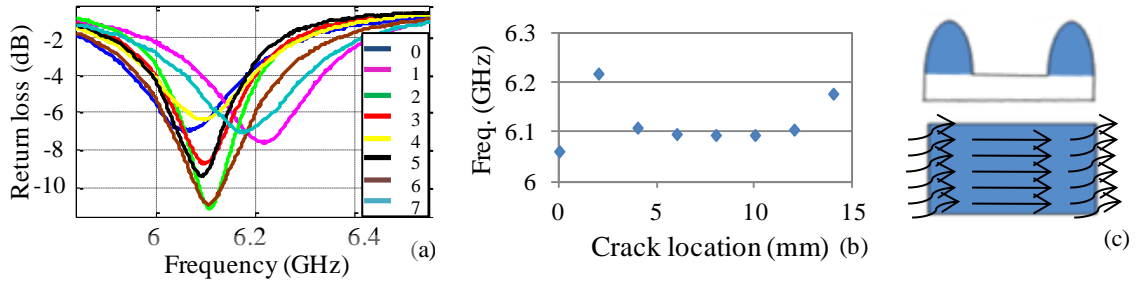


Figure 3.6: Effect of crack growth on  $f_{01}$  frequency of antenna sensor at 300 lbs; (a)  $S_{11}$  curves at different crack tip locations; (b)  $f_{01}$  frequency vs. crack tip location; (c) current density pattern of  $TM_{01}$  radiation mode.

### 3.2 Improving the Reliability of Antenna Sensor

During the fatigue experiment, the patch antenna sensor was subjected to high fatigue cycling associated with large deformations. As a result, the substrate and the patch displayed signs of either debonding or wear/tear of the patch if special fatigue-rated epoxy was not used. To improve the reliability of sensor skins, we proposed to introduce a flexible layer between the host structure and the sensor skin so that the strain transfer from the CT specimen to the antenna patch can be reduced. This section presents the design of the flexible layer based on strain transfer analysis as well as the fabrication of the flexible layer and the experimental results that validated the improvement of the sensor reliability.

#### *3.2.1 Design parameter selection*

In our crack detection experiments, we observed that the Kapton started to show signs of wear/tear or debonding only after the crack length underneath the radiation patch was longer than 6 mm, which corresponds to a crack opening of 21.1  $\mu\text{m}$  at the edge of the Kapton based on the equations provided by the ASTM standard. Therefore,

we estimated that the maximum crack opening the Kapton can sustain is  $21.1 \mu\text{m}$ . It is desired that the antenna sensor should remain intact until the crack propagates through the entire length, which corresponds to a crack opening of  $48 \mu\text{m}$ . Therefore, the flexible layer should reduce the crack opening from  $48 \mu\text{m}$  to  $21.1 \mu\text{m}$  which corresponds to a reduction of 43.9% to eliminate sensor damage.

### 3.2.2 Strain transfer analysis

In order to design the flexible layer, numerical simulation of the strain transfer from the specimen to the antenna sensor was performed using commercially available software ANSYS<sup>TM</sup>. The geometrical model shown in figure 3.7(a) is identical to the CT specimen used in the fatigue crack detection experiments. The geometry was designed in Pro-Engineer and imported to ANSYS in IGES<sup>®</sup> format for strain analysis. The crack in the specimen was simulated as a small gap of 50 microns between the joining surfaces. The origin of the coordinate systems was set at the tip of the crack

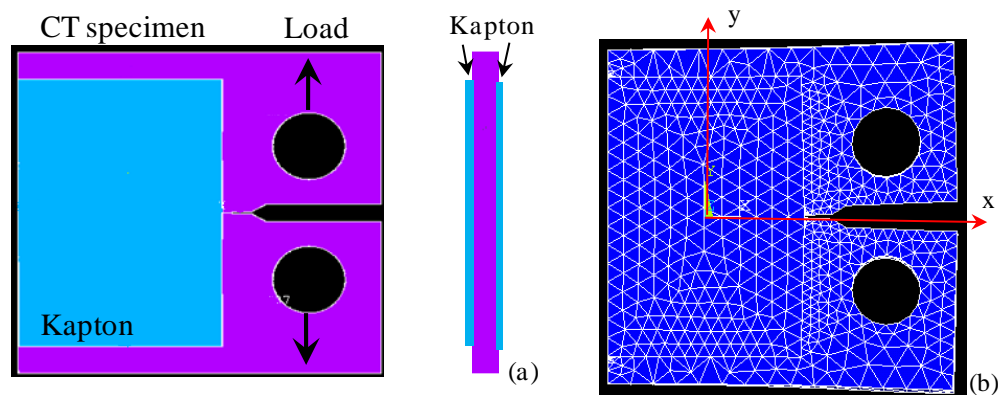


Figure 3.7: Simulation model; (a) Kapton layer bonded on both sides of the specimen; (b) meshing of the simulation model

with the positive x-axis aligned with the crack. The material was assumed to be aluminum 7075-T6 (Young's modulus = 10000 ksi and Poisson's ratio = 0.33). Two thin layers representing the dielectric substrate (2 in. long and 1.5 in. wide, 75  $\mu\text{m}$  thick) were bonded on both sides of the specimen to attain symmetry. These layers overlap the crack by 0.7 inch and they were assigned the properties of Kapton FN<sup>®</sup>. A linear-elastic isotropic element type was used for specimen whereas a non-linear element with curve-fit material properties was used for dielectric substrate. Non-conformal meshing was employed to produce the fine mesh around the crack (see figure 3.7(b)). The nodes on the bottom surface of the dielectric layer were bonded to the nodes on the top surface of specimen using the VGLUE command, which transfer the strain from the top surface of the specimen directly to the bottom surface of the dielectric substrate. A point load of 600 lbs was applied to the specimen. Figure 3.8(a) compares the  $\epsilon_{yy}$  strain on the inner and outer surfaces of the dielectric layer along the x- axis. The substrate experiences relatively small strains for the first 0.5 inch, beyond which the strains increase suddenly. This drastic increase in strain is due to the non-linear behavior of the substrate material. The strain transferred from the bottom surface to the top surface of the substrate is about 89%. In order to reduce the total strain transfer, a Polydimethylsiloxane (PDMS, Young's modulus = 262 psi, Shear modulus = 3.931 ksi, Poisson's ratio = 0.45 and incompressibility factor = 0.14429) layer was added between the specimen and Kapton. In order to quantitatively evaluate the change in strain transfer due to the added PDMS layer, three thicknesses, i.e. 30, 50, and 70  $\mu\text{m}$ , were simulated. The strain transfer reductions for these three thicknesses are compared in figure 3.8(b). As expected, the

strain transfer reduction increased with the thickness of the flexible PDMS layer. The strain transfer reduction also increased with the level of strain, as evidenced by the large strain transfer reduction at locations far from the crack tip. The respective maximum strain reduction for the 30, 50 and 70  $\mu\text{m}$  PDMS layers is 12.9%, 31.86%, and 39.95%; all occur at the furthest location from the crack tip.

Based on this estimation and the data presented in figure 3.8(b), a PDMS substrate of 70  $\mu\text{m}$  (corresponding to a strain reduction of 39.9%) may be sufficient to obtain the desired strain reduction.

### 3.2.3 PDMS fabrication and specimen preparation

To control the thickness of the PDMS layer, the PDMS layer was fabricated on a silicon wafer using traditional semiconductor fabrication process (Quirk and Serda 2000, Nanogaki 2008). The wafers were first cleaned thoroughly in ultrasonic acetone bath for ten minutes to remove any dirt particles. The cleaned wafer was spin coated with a layer of positive photo resist S1813 at a speed of 1500 rpm for 30 sec, producing a film thickness of 1.5 microns. After hard baking the wafer on a hot plate at 100<sup>0</sup>C for

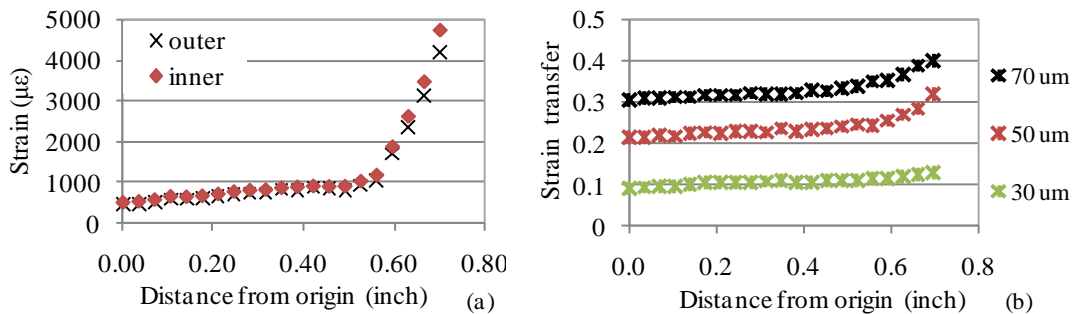


Figure 3.8: Strain transfer from specimen to Kapton; (a) without PDMS layer; (b) with PDMS layers of different thickness.

60 sec, a thin layer of PDMS was spin coated on the wafer at a speed of 1000 rpm for 60 sec. This produces a 70 micron thick PDMS layer on the wafer (Zhang *et al* 2004, Schneider *et al* 2009). After baking the wafer at 100<sup>0</sup>C for 60 seconds, the wafer was removed from the hot plate and left to cool until it reaches room temperature. The cooled wafer was then dipped in an acetone bath. Acetone reacts with the photo resist layer and separates the PDMS from the wafer. The PDMS sheet floating on the acetone was then carefully picked up with a pair of tweezers. Any acetone left on the PDMS sheet was removed with nitrogen gas.

The fabricated PDMS sheet was placed just besides the precrack and bonded to the CT specimen. Subsequently, a rectangular dielectric substrate (Kapton FN 300FN929, 2 in. x 1.5 in.) was bonded to the PDMS layer. To ensure good bonding, the surfaces of the Kapton film were slightly sanded. Fatigue rated glue (M-bond AE 15) was used to bond both the PDMS and the Kapton film. The patch antenna sensor is then fabricated over the kapton sheet. The copper strip was oriented in such a way that the pre-crack was aligned with the center line of its width direction and the pre-crack tip was at a distance of 0.2 inches from the patch. It was observed that the inclusion of the PDMS layer between the specimen and

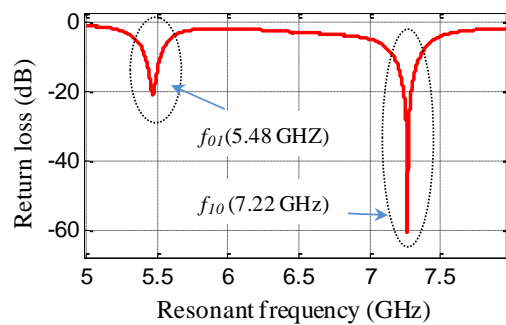


Figure 3.9: Measured  $S_{11}$  parameters of the fabricated antenna sensor

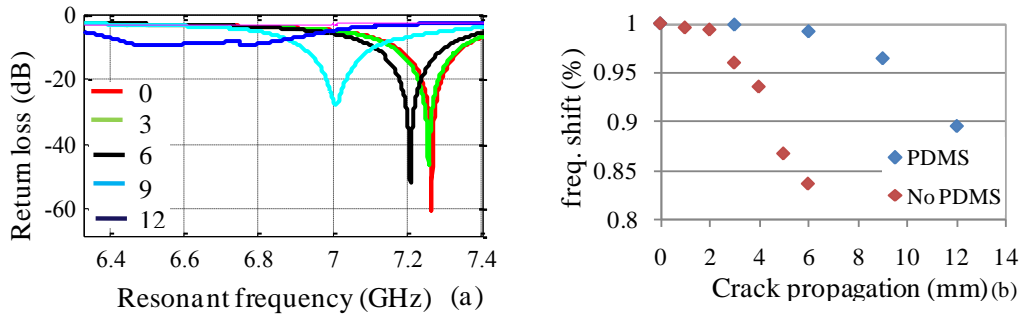


Figure 3.10: Effect of PDMS on crack-induced frequency shift of the antenna sensor; (a)  $f_{10}$  frequency shift at various crack lengths; (b) frequency shift vs. crack tip locations.

Kapton substrate did not alter the resonant parameters of the antenna sensor. As shown in figure 3.9, the antenna sensor displayed two resonant frequencies,  $f_{01} = 5.48$  GHz and  $f_{10} = 7.22$  GHz. Since the crack is perpendicular to the width direction of the antenna patch, it is expected that  $f_{10}$  frequency shifts towards the lower frequency with the crack propagation.

### 3.2.4 Results and analysis

Detailed descriptions on the fatigue test of the antenna sensor can be found in sections 3.1.2 and 3.1.3. The frequency shifts of the antenna sensor at different crack lengths are shown in figure 3.10(a). The rightmost curve (in red color) represents the resonant frequency of the antenna sensor when the crack tip just reached the antenna patch, i.e., there was no overlap between the crack and antenna sensor. Each subsequent shift of the curve is equivalent to 3 mm of crack propagation. As expected, the  $f_{10}$  of the antenna sensor shifted towards lower frequencies as the crack length increased. To determine the sensitivity of the antenna sensor to crack growth, the resonant frequency shift of the antenna sensor is plotted versus the crack propagation in

figure 3.10(b). Figure 3.10(b) also shows the data obtained from the test when the Kapton was directly bonded to the specimen (Mohammad and Huang 2011). By adding the PDMS layer, the antenna sensor was functional even after the crack had propagated through its entire length. This confirms that the introduction of the flexible PDMS layer can improve the reliability of the antenna sensor. However, the overall sensitivity of the antenna sensor was lower when the PDMS layer was added. Further investigation is needed to understand the effect of PDMS layer on the antenna sensitivity.

### 3.3 Crack Orientation Detection

In section 3.1, we presented a patch antenna sensor which can effectively detect crack propagation with sub-millimeter resolution (Mohammad and Huang 2010, Deshmukh and Huang 2010, Deshmukh *et al* 2010). Fatigue loading was applied on Compact Tension (CT) specimen to propagate the cracks. Due to the slow crack propagation rate in a CT specimen, it took about two days to complete one experiment. In addition, numerical simulation of a realistic fatigue crack using a commercially available Electromagnetic (EM) simulation tool such as Sonnet Pro was very time-consuming because of the small crack opening near the crack tip. These two limitations prohibit a detailed parametric study on the capability of the antenna sensor to detect crack orientation through fatigue testing of the CT specimen. In this study, we developed an experimental procedure to study the effect of the crack orientation on the resonant frequencies of the antenna sensor. The fatigue crack was imitated as a 0.7 mm wide slot machined in the ground plane of the antenna sensor. Compared to fatigue testing, this approach allowed us to conduct a large number of experiments in a short

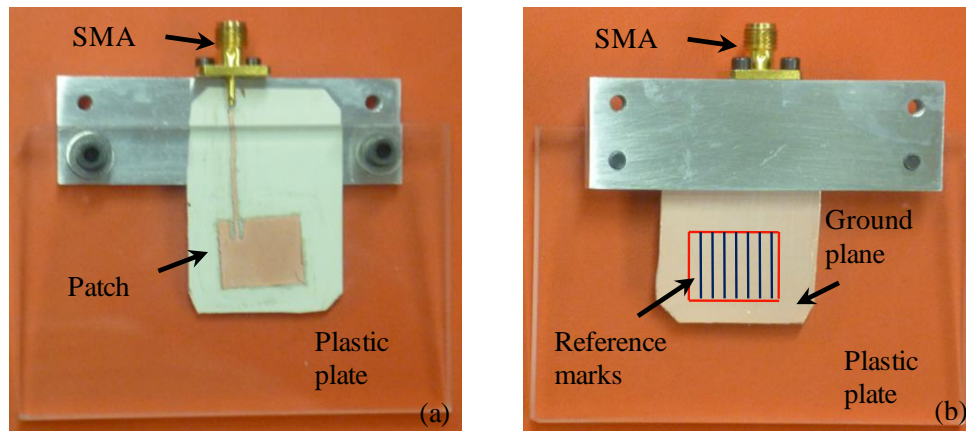


Figure 3.11: Fixture for crack propagation and monitoring; (a) SMA/patch antenna sensor assembly; (b) reference marks on the ground plane of the antenna sensor.

duration of time. In addition, realistic numerical simulation models can be easily established to validate the experimental results. Based on this approach, the capability of the antenna sensor for crack orientation detection can be investigated in detail.

### 3.3.1 Fabrication of antenna sensor for crack orientation detection

The antenna sensors were fabricated on a laminate board with a dielectric constant  $\epsilon = 3.66$  and  $35 \mu\text{m}$  thick copper films on both sides (Rogers 4350B). After cutting the laminate board into 2 inch long and 1.5 inch wide rectangular pieces, the antenna patch was milled on one side of a laminate board using a mini-milling machine, Turbo carver. The outline of the antenna patch was first formed on the laminate with a fine cutter (0.1 mm thick), followed by machining off the copper surrounding the antenna patch with a wider cutter. The copper on the other side of the laminate, which forms the ground plane of the antenna sensor, was left intact. After masking the antenna patch and the ground plane with a strain gage tape, the board was dipped in Ferric Chloride solution for ten to fifteen minutes to etch off the remaining copper

around the antenna patch. Once the copper was completely etched, the laminate was rinsed thoroughly in water and dried. The masking tape was then removed and the antenna sensor was thoroughly cleaned with acetone to remove any residual taping. To connect an SMA connector to the antenna sensor, the antenna sensor was sandwiched between an aluminum block and a plastic plate. The SMA connector was then mounted on the aluminum block with its pin touching the end of the antenna sensor feed line. Figure 3.11 (a) shows the SMA/antenna sensor assembly. To facilitate measuring the crack length visually, the location of the antenna patch was marked on the ground plane and reference marks were drawn at regular intervals of 2 mm (see figure 3.11(b)). The antenna sensor can then be connected to a Vector Network Analyzer (VNA, Rohde & Schwarz, ZVA 24) through the SMA connector to measure the  $S_{11}$  parameter of the antenna sensor.

### 3.3.2 Experiment setup for crack orientation detection

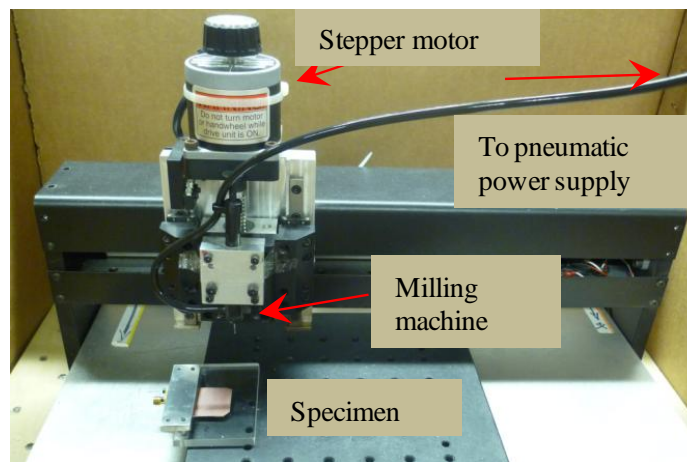


Figure 3.12: SuperScribe circuit prototyping system

To study the effect of crack propagation and orientation on the resonant frequencies of the antenna sensor, thin slots (0.7 mm width) were machined in the ground plane of the antenna sensor to imitate the cracks. The experimental setup to machine the crack using a milling machine is shown in figure 3.12. The milling machine was custom-made by mounting a high speed pneumatic carver (Turbo carver TC550) on a SuperScribe™ Circuit Board Prototyping System from Micro Kinetics Corporation. The vertical depth of the cutting tool was precisely controlled to be 35  $\mu\text{m}$ , which corresponds to the thickness of the ground plane. The SMA/sensor assembly, shown in figure 3.11(b), was placed underneath the cutting tool with its antenna patch facing down so that cracks can be milled in the ground plane of the antenna sensor. The crack was initiated at one of the edges of the antenna patch. Whenever the crack reached a reference mark, the antenna sensor assembly was removed from the milling machine and the  $S_{11}$  parameter of the antenna sensor was measured on a VNA. The antenna sensor was then again placed under the milling machine and measurements were done at each reference mark until the crack passes through the entire length of the antenna patch.

### 3.3.3 Experiment configurations

Four different crack configurations were studied with the method described above (see figure 3.13). The first configuration was a crack parallel to the length direction of the antenna patch and at a distance  $d$  from the horizontal center line. This configuration is chosen to be the same as those we tested in the fatigue experiments (Deshmukh *et al* 2010) so that the experiment results obtained from this study can be

compared with those from previous study. The second configuration was a crack that propagated along the diagonal direction of the antenna patch. The third configuration is a set of cracks that have various inclination angles relative to the length direction of the patch and the last crack configuration is a kinked crack that propagated along the length direction first and then propagated at various angles relative to length direction. The  $S_{11}$  resonant parameters of the antenna sensor were measured for each case and the shift of the antenna  $f_{10}$  and  $f_{01}$  frequencies with the crack propagation were analyzed and compared with the simulated results. The simulated antenna radiation patterns for different crack lengths and orientation were also studied to obtain qualitative understanding of the effect of crack orientation on the antenna resonant frequencies.

### 3.3.4 Simulation model

The antenna design was simulated using a commercial program HFSS<sup>TM</sup>. In the simulation setup, a vacuum box of 100mm x 100mm x 50mm was created (see figure

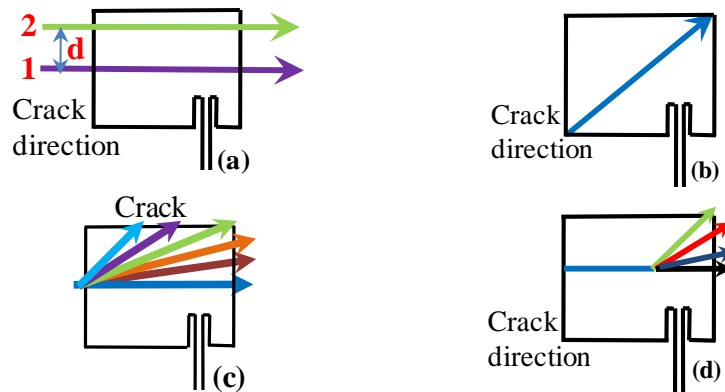


Figure 3.13: Crack configurations; (a) crack parallel to the length and at a distance  $d$  from center line; (b) crack along the diagonal of the patch; (c) cracks at various inclination angles; (d) kinked cracks.

3.14(a)). The patch antenna, ground plane and the patch were added to the simulation model inside the vacuum box. The substrate was assumed to have a relative permittivity of 3.4 and a relative permeability of 1. The antenna patch and the ground plane are assumed to be made of perfect electric conductors; the patch has zero thickness whereas the ground plane was 66  $\mu\text{m}$  thick. The antenna patch was excited at the end of the microstrip line with a 50-ohm lumped port. The size of the spatial cells in HFSS discretization was roughly  $\lambda_d/10$ , where  $\lambda_d$  is the wavelength corresponding to the dielectric substrate's material. The dimensions of the patch antenna sensor with the inset feed line is shown in figure 3.14(b). The patch antenna was first simulated without any cracks on the ground plane. The crack in the ground plane of the antenna

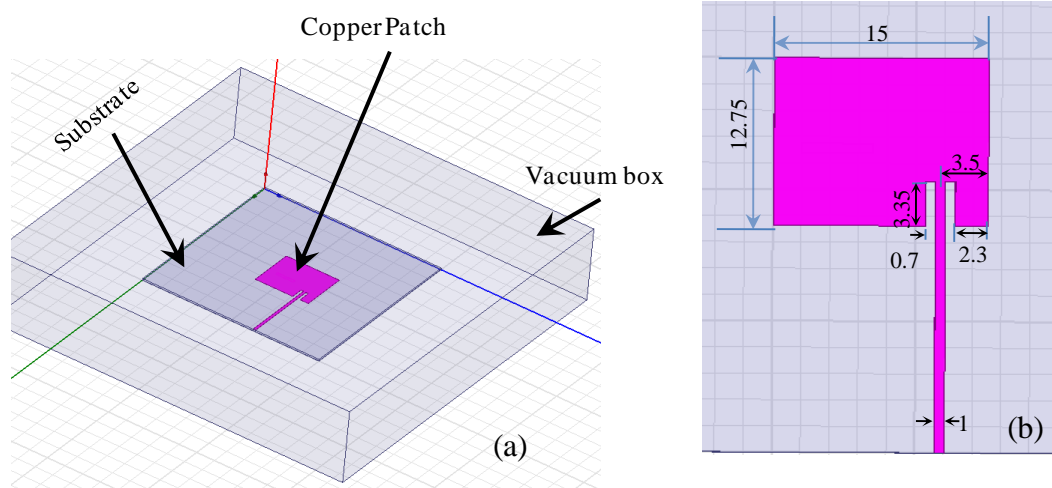


Figure 3.14: (a) simulation model of the patch antenna in HFSS<sup>®</sup>; (b) design of patch antenna sensor (All dimensions are in mm)

sensor was simulated by introducing a 0.7 mm wide rectangular slot at the desired

orientation on the ground plane layer of the simulation model. The simulation and experimental results are compared and analyzed in the next section.

### 3.3.5 Results and analysis

Two cracks were studied for the 1<sup>st</sup> crack configuration. As shown in figure 3.15(a), crack “1” passes through the center of the antenna patch while crack “2” is offset from the center by a distance  $d = 5$  mm. The shift of the measured  $S_{11}$  curves with the growth of crack “1” is shown in figure 3.15(b). The right most curve (the blue curve) represents an overlapping crack length of 0 mm, i.e., the crack has just reached the left edge of the antenna patch. The leftmost curve (the black curve) was obtained when the crack has propagated through the entire patch. Each sequential  $S_{11}$  curve in between these two curves represents a crack propagation of 4 mm. Similar to what we have observed in fatigue experiment (Deshmukh *et al* 2010), the  $f_{10}$  resonant frequency shifted towards the lower frequency while the  $f_{01}$  resonant frequency remained almost constant. The measured  $f_{10}$  and  $f_{01}$  frequencies of the antenna sensor at various crack tip positions are compared with the simulated results in figure 3.15(c). We can see that the experimental results matched well with the simulation results for both resonant frequencies. Figure 3.15(d) compares the  $f_{10}$  and  $f_{01}$  frequency shifts of the antenna sensor containing crack “2” with the frequencies of the sensor containing crack “1”. We observe that the slope of the frequency shift is the same for both cases, implying the antenna sensor can detect both cracks with similar sensitivity. However, crack “2” will not be detected until it is 2 mm past the left edge of the antenna patch. This phenomenon can be explained by studying the current distribution pattern of the  $TM_{10}$

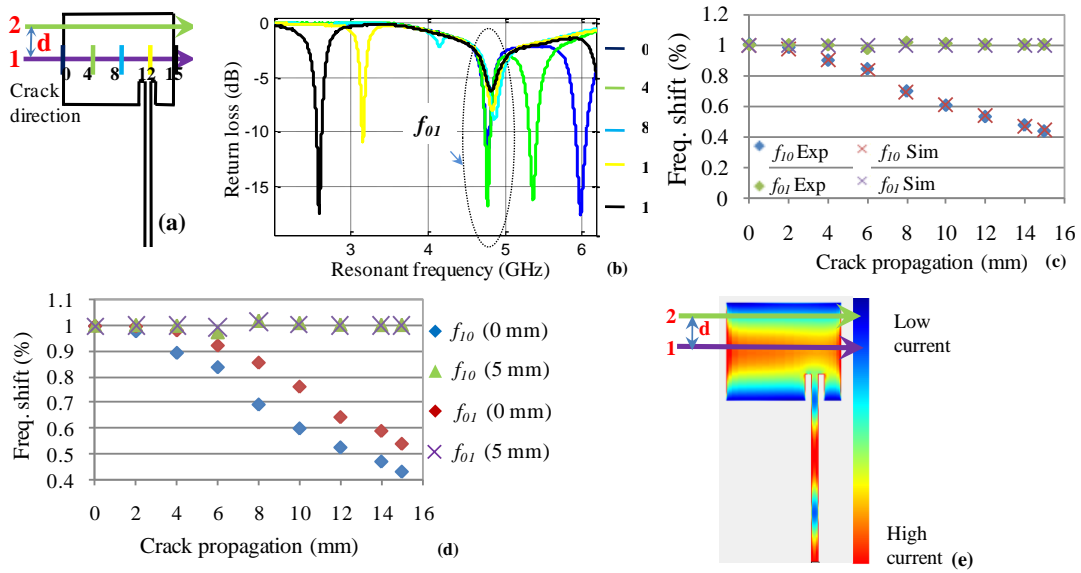


Figure 3.15: Effect of a crack passing perpendicular to the width at an offset to the center of the patch; (a) crack configuration; (b) shift of  $S_{11}$  curves with crack growth; (c) experimental and simulated  $f_{10}$  and  $f_{0l}$  frequencies at different crack tip locations; (d) effect of crack offset on the resonant frequency shift; (e) current distribution along  $TM_{10}$  radiation mode

radiation mode. As shown in Figure 3.15(e), the current density along the  $TM_{10}$  mode is much higher at the center of the patch and gradually reduces toward the edges of the antenna patch (Horng *et al* 1994). The crack propagating along the center line disturbs the high current density region. As a result, it causes a frequency shift as soon as it is underneath the antenna patch. On the contrary, a crack that is at a distance from the center line of the antenna patch passes through the low current density region. Therefore, a longer crack length is required to cause an observable frequency shift. An antenna sensor with a smaller width dimension may help reducing this blind zone (Xu and Huang 2011). The  $f_{0l}$  resonant frequency remained constant in either case because the current along the length direction was not disturbed.

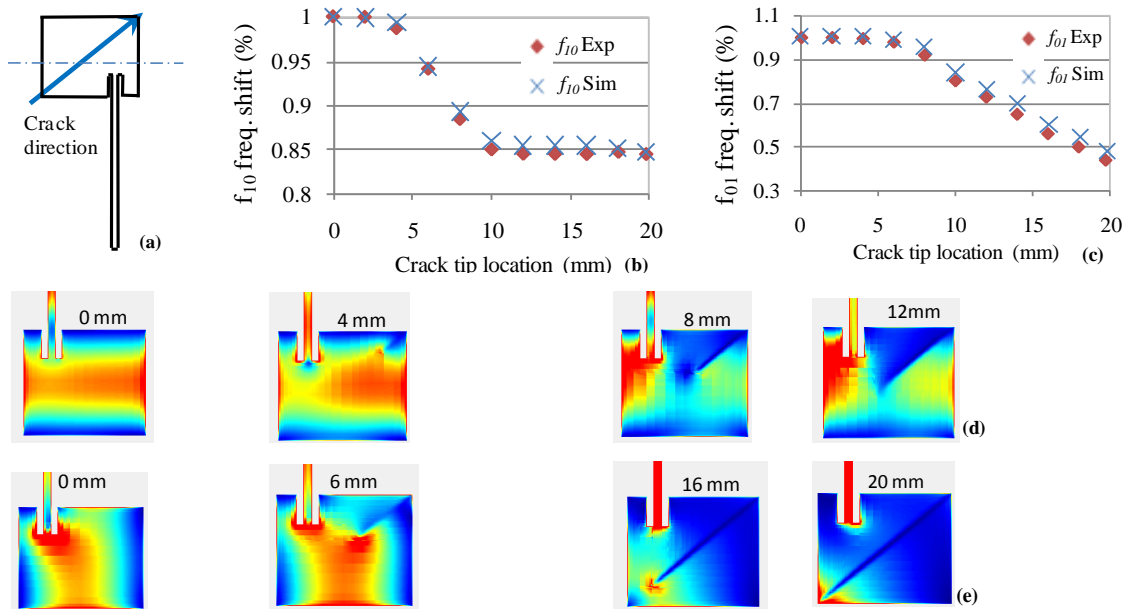


Figure 3.16: Effect of diagonal crack on the antenna sensor; (a) crack configuration; (b)  $f_{10}$  resonant frequency shift vs. crack tip locations; (c)  $f_{01}$  resonant frequency shift vs. crack tip locations; (d)  $TM_{10}$  mode current distribution with a diagonal crack; (e)  $TM_{01}$  mode current distribution with a diagonal crack.

In order to evaluate the capability of the antenna sensor to detect the crack orientation, a crack was introduced along the diagonal of the antenna patch (see figure 3.16(a)). Both the  $f_{10}$  and  $f_{01}$  frequencies of the antenna sensor, once again obtained from the  $S_{11}$  curves, are plotted against the crack tip locations in figure 3.16(b) and 3.16(c). The total length of the diagonal crack underneath the patch is around 19.87 mm (diagonal length for a patch 15.25 mm long and 12.75 mm wide). As expected, both the resonant frequencies shifted towards the lower frequency as the crack propagated under the antenna patch. The  $f_{10}$  resonant frequency, as shown in figure 3.16(b), has two dwell regions and one high sensitivity region. This phenomenon can be explained again with the current distribution of the  $TM_{10}$  radiation mode shown in

figure 3.16(d). Whenever a crack is propagated diagonally, it initially propagates through the lowest current density region, which results in a lower frequency shift. This justifies the first dwell region. After 4 mm of crack propagation in the low current density region, the crack enters the high current density region. As a result, the  $f_{10}$  resonant frequency starts to shift towards the lower frequency. The crack propagation also changes the current distribution of the  $TM_{10}$  mode. At a crack length of 8 mm, the high current region is “pushed” to the left side of diagonal crack. When the crack reaches 12 mm, the current is confined in the left-top corner of the antenna patch. As a result, further increase in crack propagation does not affect the current density distribution much. This explains the second dwell region in the  $f_{10}$  resonant frequency shift. On the other hand, the  $f_{01}$  resonant frequency has one dwell region only. To gain a better insight on the  $f_{01}$  resonant frequency, the  $TM_{01}$  radiation mode was studied. Figure 3.16(e) represents the current distribution along the  $TM_{01}$  radiation mode of the antenna sensor. It can be observed that the current density is higher along the horizontal edges, around the inset feed and at the center of the patch antenna. The resonant frequency of the antenna sensor is almost constant for the first 6 mm of crack propagation due to the low current density region at the corner of the patch. As the crack propagates beyond 6 mm, it enters the high  $TM_{01}$  current density region thereby causing the  $f_{01}$  frequency to shift towards the lower frequency. As the crack propagates, the high current density region is shifted along with the crack. This explains why the  $f_{01}$  resonant frequency continues to shift towards the lower frequency even after the crack propagates beyond the original high current density region. For a diagonal crack longer

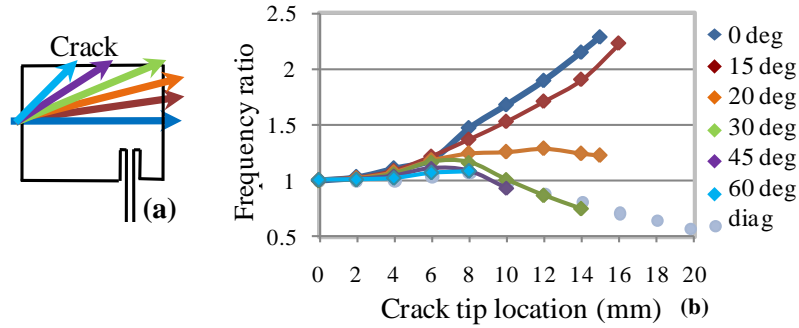


Figure 3.17: Effect of various inclination angles on antenna frequency; (a) schematic of crack propagation; (b) frequency ratio vs. crack tip locations.

than 4 mm, the crack will be detected as an inclined crack since both resonant frequencies were modified. Again, a small antenna patch will help reducing the dwell regions.

The effect of a crack on the structural integrity depends on the relative inclination angle between the loading direction and the crack propagation. It is therefore very important for a sensor to detect the inclination angle of a crack. To evaluate the effect of inclined cracks on the resonant frequencies of the antenna sensor, the crack was initiated at the middle point of the antenna's left edge and then propagated at five different inclination angles (15, 20, 30, 45 and 60 degrees)(see figure 3.17(a)). Similar to the previous experiments, both the  $f_{10}$  and  $f_{01}$  frequencies of the antenna sensor were obtained from the  $S_{11}$  curves. However, analyzing two different frequencies ( $f_{10}$  and  $f_{01}$ ) to evaluate the crack position and orientation angle was tedious. To simplify the data processing, a single parameter  $R$  is introduced to represent the effect of the crack on the two resonant frequencies.  $R$  is defined as the ratio between the normalized  $f_{01}$  and  $f_{10}$  frequencies, where the resonant frequencies at a given crack

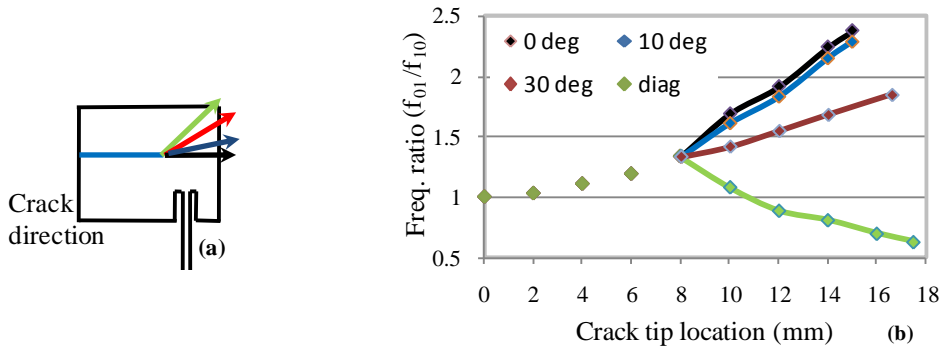


Figure 3.18: Effect of crack kinking on the antenna frequency; (a) schematic of crack propagation; (b) freq. ratio vs. crack tip locations.

length are normalized by their counterparts at zero overlapping crack length. Figure 3.17(b) shows the frequency ratio  $R$  at various crack tip locations. For small inclination angles, the frequency ratio increases with the crack propagation. This is due to the fact that the  $f_{10}$  frequency reduces with the crack propagation while the  $f_{01}$  frequency remains almost constant. For the large angles, the frequency ratio reduces with the crack propagation since the  $f_{10}$  frequency shift is higher than the  $f_{01}$  frequency shift. Each inclination angle corresponds to a unique frequency ratio trend. Therefore, by tracking the change of the frequency ratio  $R$ , the crack propagation and orientation can be determined. Figure 3.17(b) also includes the effect of a diagonal crack, i.e. 2<sup>nd</sup> crack configuration, on the frequency ratio. As the diagonal crack has an inclination angle of 40 degrees to the length direction of the patch, the frequency ratio trend looks similar to that of a 45 degree inclined crack. However, the total crack propagation is much longer as the crack was initiated at the bottom of the patch.

In realistic scenarios, a crack may initially propagate along one direction and then change its propagation direction. These kinked cracks sometimes could be very

dangerous because it might change the crack propagation pattern completely. In order to evaluate the effect of a kinked crack on the antenna sensor, a straight crack propagating along the length direction centerline was introduced. The orientation of the crack was then changed to propagate along different angles (10, 30, 40 degrees) after it reached the center of the antenna patch (see figure 3.18(a)). Again, both the frequencies were obtained from the  $S_{11}$  curves and the frequency ratio  $R$  at various crack tip locations was plotted in figure 3.18(b). Since the crack is parallel to the length of the antenna patch for the first 8 mm, the frequency ratio trend is similar in all the three experiments. Once the crack changes its orientation, the frequency ratio changed accordingly. The trend for the 0 degree and 10 degree angles matched very well with the trend presented in figure 3.17(b). The trend for the 30 and 40 degree angles are slightly different from those in figure 3.17(b). This is probably due to the radiation current density changes caused by the first 8 mm of straight crack growth. Nonetheless, figure 3.18 clearly indicates that the crack kinking can be detected and measured from the frequency ratio  $R$ .

Based on this, a parametric study investigating the effect of crack orientation and propagation on the resonant frequencies of the antenna sensor was performed. A single parameter, i.e. the normalized frequency ratio  $R$ , is introduced to represent the effect of crack on the two resonant frequencies of the antenna sensor. The change of the normalized frequency ratio  $R$  with the crack growth provides a unique indication of the crack orientation. Therefore, the orientation of the cracks in the ground plane of the antenna sensor can be monitored from the frequency ratio. The experimental results were validated using numerical simulations. We also discovered that the simulated

radiation pattern provides qualitative explanation of the crack-induced frequency shift. The antenna sensor cannot differentiate cracks that are symmetric about the centerline of the antenna patch. In this case, the knowledge of the loading condition may assist identifying the actual crack growth direction.

### 3.4 Wireless Interrogation of Hidden Cracks

Recently, our group demonstrated a wireless interrogation technique that can detect a patch antenna sensor when it is under the line-of-sight illumination of an interrogation antenna. Additional details on the wireless interrogation technique can be found in the literature (Deshmukh and Huang 2011). As a part of my PhD study, I developed a wireless interrogation technique that can interrogate the antenna sensor when it is placed out of the line-of-sight of the interrogation antenna. The aim of this technique is to detect cracks between lap joints or in any other scenario where a crack is hidden between two parts of a structure. The implementation of the wireless interrogation unit using commercially available microwave components is presented in detail. The experimental results were compared with the wired measurements and

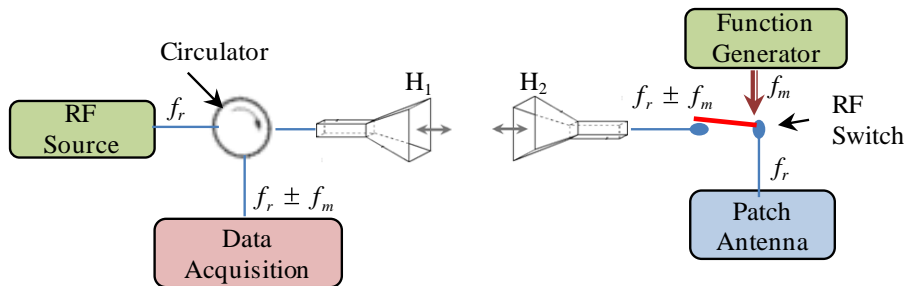


Figure 3.19: Patch antenna sensor and the data acquisition system.

confirmed the capability of this technique to wirelessly interrogate any hidden cracks.

### *3.4.1 Principle of operation*

The principle of operation of the wireless interrogation technique to interrogate the patch antenna sensor when it is placed out of line-of-sight of the interrogation antenna is discussed here in detail. An interrogation signal  $f_i$  is transmitted from the horn antenna  $H_1$  to horn antenna  $H_2$ , which is then routed to the patch antenna sensor. The patch antenna sensor will partially receive the interrogation signal and the signal that is not received by the antenna sensor is reflected back to the horn antenna  $H_2$ . The amount of signal received by the antenna sensor depends on the antenna sensors' operation bandwidth and the corresponding return loss. When the interrogation signal matches with the resonant frequency of the antenna sensor, most of the energy is received by the antenna sensor. As a result, the signal reflected to the horn  $H_2$  is weak. On contrary, when the interrogation frequency and the antenna resonant frequency do not match, very little energy is received by the antenna sensor. As a result, a stronger signal is reflected to the horn antenna  $H_2$ . Therefore by sweeping the frequency of the interrogation signal, the antenna frequency can be identified from the frequency-strength relationship of the reflected signal. Unfortunately, the structures surrounding the horn antenna also reflect the interrogation signal and thus create structural backscattering. Because the structural backscattering is independent of the antenna frequency and usually is much stronger than the antenna backscattering, we need to resort to an amplitude modulation circuit to isolate the antenna backscattering from the structural mode. As shown in figure 3.19, a RF switch is added between horn  $H_2$  and

the antenna sensor to accomplish the amplitude modulation. When the switch is open, the entire received signal will be reflected at the switch and causes a large backscattering. When the switch is closed, the signal reaches the antenna sensor and part of the energy is reflected to the horn antenna  $H_2$ .

If the RF switch is controlled by a square wave with a frequency of  $f_m$ , the frequency of the amplitude modulated backscattered signal will be  $f_i \pm f_m$ . This creates additional frequency bands that are offset from the interrogation frequency  $f_i$ . When the interrogation frequency is near the resonant frequency of the antenna sensor, we have a large difference in the amplitudes of the backscattered signals at the two switching states (see figure 3.20(a)), resulting in a large sideband. As the interrogation

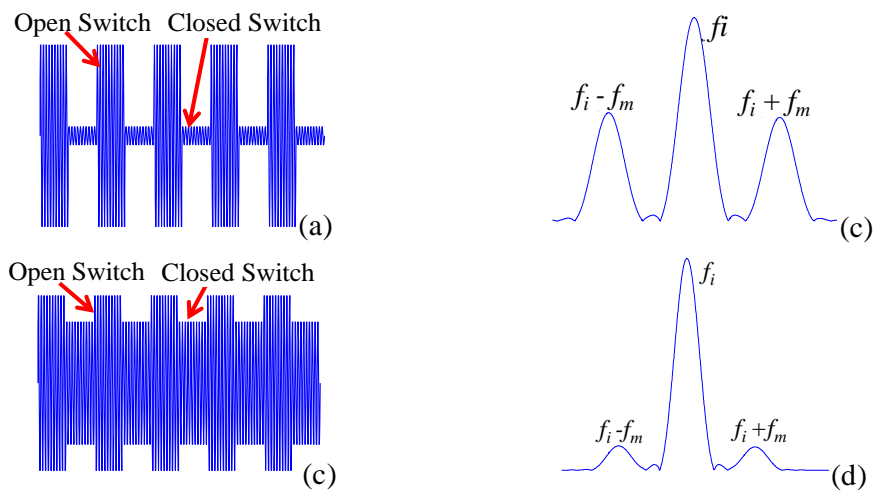


Figure 3.20: (a) & (b) time and frequency domain representation of the backscattered signal when the interrogation frequency is close to the antenna resonant frequency; (d) &(e) time and frequency domain representation of the backscattered signal when the interrogation frequency is away from the antenna resonant frequency.

signal moves away from the resonant frequency of the patch antenna, the difference in the amplitudes of the backscattered signal between the two switching states is smaller, which produces a smaller sideband (see figure 3.20(c)). Therefore, the antenna resonant frequency can be identified as the interrogation frequency at which the amplitude of the sideband is the maximum. Since the RF switch and the patch antenna are passive, the only component that needs power is the function generator. However, the function generator can be replaced with a low frequency oscillator that operates at very low power and can be powered with an energy harvesting device (Xu and Huang 2012). Therefore, the antenna sensor can be interrogated without a local power supply or a battery.

#### *3.4.2 Experimental setup*

The experimental setup for the wireless interrogation of the antenna sensor assembled using commercially available components is illustrated in figure 3.21. A 0 dbm microwave signal was generated by a RF signal generator (Anapico, APSIN20G). The RF signal is transmitted to the horn antenna  $H_2$ , located at a distance of 1.3 meters away from  $H_1$ . The RF switch used in the setup is a Pseudomorphic High Electron Mobility Transistor (pHEMT) (Avago, ATF-36077). The backscattered signal is received by the horn antenna  $H_1$  and routed to a high speed oscilloscope (Lecroy SDA 760Zi) through a circulator (DiTOM, D3C 4080) where the signal is analyzed and recorded.

#### *3.4.3 Experimental procedure*

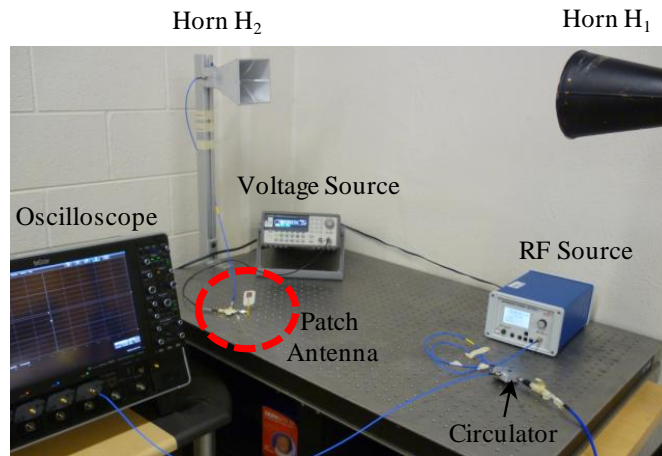


Figure 3.21: Experimental setup for remote interrogation of patch antenna sensor.

To evaluate the feasibility of interrogation technique to monitor crack propagation wirelessly, thin slots (0.7 mm width) were machined in the ground plane of the patch antenna sensor to imitate the cracks (Mohammad and Huang 2011). The cracks were machined with a hand-held high speed pneumatic carver (Turbo carver TC550). Reference marks were marked on the ground plane of the antenna sensor at intervals of 2 mm underneath the patch prior to the experiment. The antenna sensor with machined crack tip at each reference mark was interrogated using the wireless interrogation unit.

#### 3.4.4 Experimental results and analysis

The normalized frequency-amplitude curves with different crack length are shown in figure 3.22(a). The amplitudes of the frequency-amplitude curves were normalized with respect to its maximum value for each crack length. The shifts in the resonant frequency of the antenna are clearly observed in figure 3.22 (a). The right-most curve (i.e., black curve) represents when there is no crack in the ground plane of

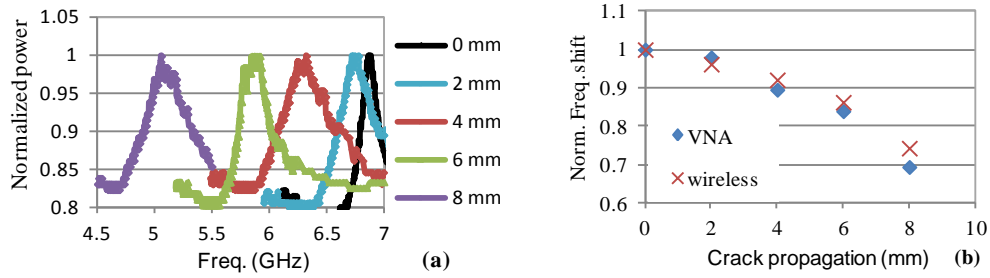


Figure 3.22: Effect of crack propagation on the resonant frequency of the antenna sensor; (a) shift of peak power with crack propagation; (b) normalized resonant frequency shift versus crack tip location.

the antenna sensor. Each subsequent shift of the curve to the left represents a crack propagation of 2 mm. The resonant frequency shift of the antenna sensor versus the crack length is shown in figure 3.22(b). For reference, the data obtained with the wireless interrogation technique was compared with the data obtained directly from a Vector Network Analyzer (VNA) (Mohammad and Huang 2010). The agreement between these two sets of measurements validates the feasibility of the wireless interrogation technique to measure the frequency shift of the antenna sensor when it is out of the sight of the interrogation antenna.

## CHAPTER 4

### SHEAR/COMPRESSING SENSING

In this chapter, we discuss the ability of the patch antenna sensor to detect shear acting on the plantar surface of the foot with an aim to study the formation, diagnostics and prevention of foot ulcers for diabetic patients. In addition to a shear detecting patch antenna sensor, the evaluation of a pressure detecting loop antenna sensor is also discussed. The sensor design, experiment setup, procedure, results and analysis for both shear and pressure detection are presented in detail.

#### 4.1 Shear Detection Sensor

The design of the shear sensor starts with selecting the maximum shear stress the sensor can experience under the foot. According to previously published work (Lord and Hosein 2000, Lott *et al* 2008, Perry *et al* 2002), the typical maximum shear stress under the foot ranges from 18 to 86.5 kPa. Therefore, we designed the shear sensor to be able to withstand a maximum shear stress of 86.5 kPa. Another consideration is the hysteresis of the substrate material. We experimentally characterized the hysteresis of both a silicon rubber (RTV 245, Eager Polymers) and a foam material (Poron Urethane Foam, Rogers Corporation). The silicon rubber material displayed a strong hysteresis that deems it unsuitable as a sensor material while the Poron cushioning material did not exhibit any hysteresis. In addition, the Poron material is light weight, flexible, and has a higher strength. The shear modulus  $G$  of the Poron substrate was measured to be 385

kPa from a simple shear test. Assuming the maximum shear deformation of the substrate is 2 mm, the height of the substrate can be calculated to be

$$h = \frac{\delta_{max}}{\gamma} = \delta \frac{G}{\tau_{max}} = 8.9 \text{ mm} , \quad (4.1)$$

where  $\delta_{max}$  is the max shear deformation,  $\gamma$  is the shear strain,  $G = 385 \text{ kPa}$  is the shear modulus, and  $\tau_{max} = 86.5 \text{ kpa}$  is the desired maximum shear stress. Based on the calculations, the height of the Poron substrate was chosen to be 9.5 mm, a standard thickness provided by the vendor.

The effect of shear deformation on the antenna resonant frequency was simulated using a commercial program HFSS<sup>TM</sup>. As shown in figure 4.1, the antenna patch was assumed to be fabricated on a 508  $\mu\text{m}$  thick laminate substrate (Rogers RO4350), which is mounted on a 9.5 mm thick Poron substrate. The Poron substrate was assigned a relative permittivity of 1.7 while the laminate had a relative permittivity of 3.66. The relative permeability for both substrates materials was assumed to be 1. The antenna patch and the ground plane were assumed to be made of perfect electric

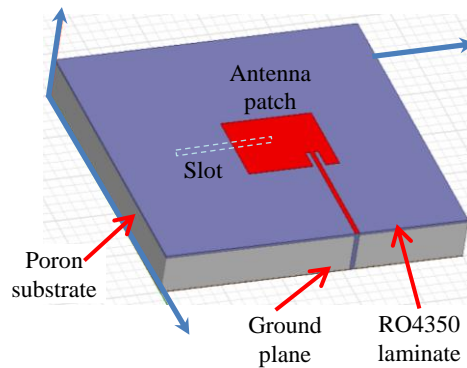


Figure 4.1: HFSS simulation model of the shear sensor.

conductors; the antenna patch had zero thickness whereas the ground plane was 5 mm thick. The size of the antenna patch, 15 mm long and 12.75 mm wide, was the same as the antennas used in our previous research (Mohammad and Huang 2010, Deshmukh et al 2010). The antenna patch was excited at the end of the microstrip feed line with a 50-ohm lumped port. The size of the spatial cells in HFSS discretization was roughly  $\lambda_d/10$ , where  $\lambda_d$  is the wavelength corresponding to the dielectric substrate's material. The resonant frequencies of the antenna sensor without a slot in the ground plane were simulated to be  $f_{10} = 5.628$  GHz and  $f_{01} = 4.59$  GHz respectively. A 0.7 mm wide rectangular slot was then introduced perpendicular to the width of the patch. The resonant frequencies of the antenna sensor were simulated for every 1 mm increase of the overlapping length between the slot and the antenna patch. The simulated relationship between the overlapping length and the resonant frequency of the antenna sensor is shown in figure 4.2. Since the relationship is fairly linear for the overlapping lengths ranging between 9 mm and 15 mm, we design the shear sensor to have an overlapping length of 9 mm at the zero shear force. The shear sensitivity of the sensor is calculated from the slope of the fitting equation as

$$\frac{\Delta f}{\Delta \tau} = \frac{\Delta f}{G \left( \frac{\Delta l}{h} \right)} = \left( \frac{h}{G} \right) \left( \frac{\Delta f}{\Delta l} \right) = 135.7 \text{ Hz/Pa.} \quad (4.2)$$

Once the design is finalized, the antenna sensors were fabricated on the laminate board with a 35  $\mu\text{m}$  thick copper films on both sides. The laminate board was first cut into 50 mm long and 20 mm wide rectangular pieces and the patch antenna sensor was replicated on one side of the laminate using press-n-peel PCB transfer film. The board

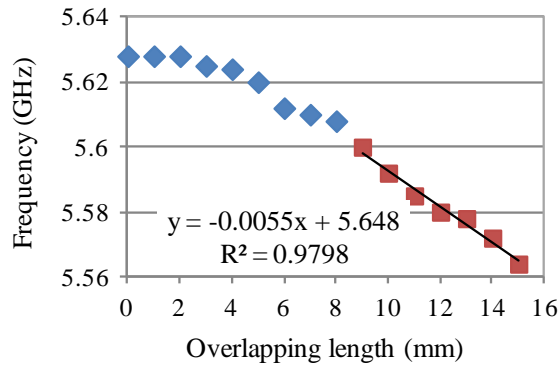


Figure 4.2: Simulated relationship between overlapping length and antenna frequency.

was then dipped in Ferric Chloride solution for ten to fifteen minutes to etch off the unwanted copper, followed by thoroughly rinsing the laminate in water and leaving it to dry completely. The Poron substrate was cut into a rectangular pillar (16 mm long and 14 mm wide) so that a shear force of 19.3 N will produce a shear stress of 86.5 kPa, which is the maximum shear stress expected to be experienced by the sensor. The final assembly of the antenna shear sensor with the pillar shaped Poron substrate sandwiched between the laminate board and the slotted ground plane is shown in figure 4.3 (a). In order to measure the  $S_{11}$  parameter of the antenna sensor using a Vector Network

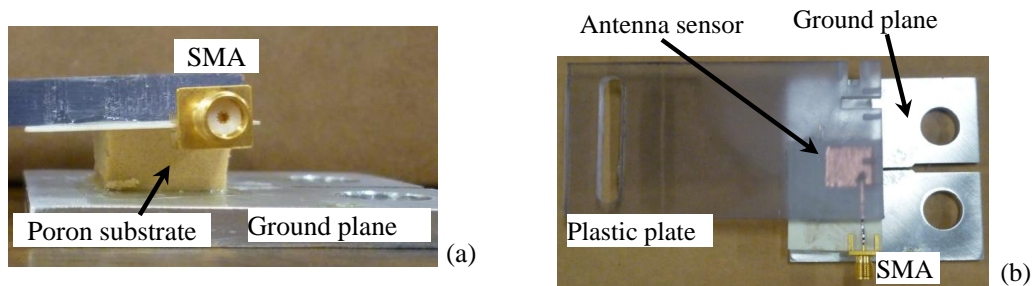


Figure 4.3: Antenna shear sensor; (a) poron substrate sandwiched between the antenna patch and the ground plane – side view; (b) SMA/patch assembly with the antenna patch shown – top view.

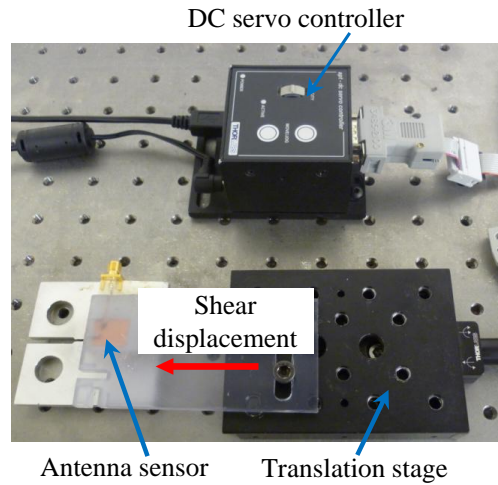


Figure 4.4: Experiment setup for shear sensing

Analyzer (VNA), and a SMA connector was installed on the laminate board with its center pin soldered to the microstrip feed line, as shown in figure 4.3(b).

#### 4.1.1 Shear detection experiment setup

The experimental setup to characterize the shear sensitivity of the antenna sensor is shown in figure 4.4. The ground plane of the antenna sensor was fixed to an optical table. In order to apply controlled shear deformation to the substrate, a plastic plate was bonded on top of the antenna sensor. The other end of the plastic plate was attached to a motorized linear translation stage controlled by a DC servo controller (Thorlabs, TDC001). The servo controller was connected to a computer USB port and operated using the apt<sup>TM</sup> software. The displacement was applied along the direction that increases the overlapping length between the antenna patch and the slot in the ground plane. The translation stage was subjected to gradual lateral displacement and the controller was stopped at intervals of 0.5 mm. The  $S_{11}$  parameters of the antenna

sensor were measured using a VNA (Rohde & Schwarz, ZVA 24) at every interval. The maximum shear displacement applied was 3 mm.

#### 4.1.2 Shear detection results and analysis

The  $S_{11}$  curves of the antenna sensor at different shear displacements are shown in figure 4.5(a). The right-most curve, i.e., black curve, was measured when the overlapping length between the slot and the antenna sensor is 9 mm. Each subsequent shift of the curve to the left corresponds to a 0.5 mm increase in shear displacement. The leftmost curve represents the  $S_{11}$  curve of the antenna sensor when the shear displacement is 3 mm. The  $f_{10}$  frequencies of the antenna sensor obtained from the  $S_{11}$  curves are plotted versus the shear displacement in figure 4.5(b). As expected, the  $f_{10}$  frequency reduced linearly as the shear displacement was increased. Compared with the simulated displacement-frequency relationship shown in figure 3, the measured antenna frequency at zero shear deformation, i.e. at an overlapping length of 9 mm is

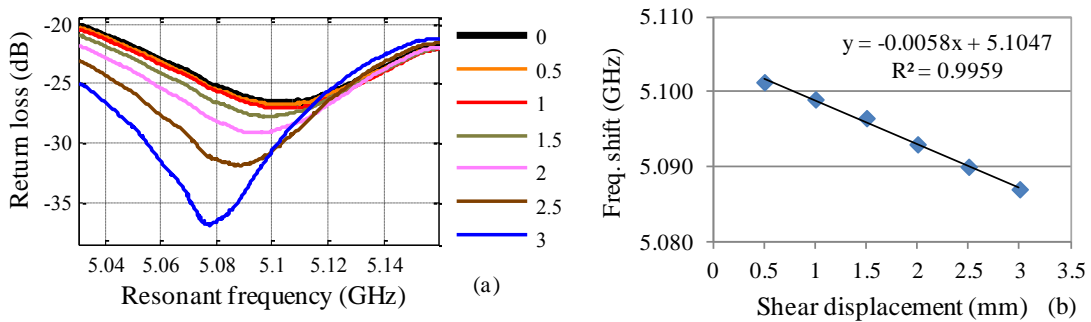


Figure 4.5: Effect of shear displacement on the resonant frequency of the antenna sensor; (a) shift of  $S_{11}$  curves with shear displacement; (b) resonant frequency shift vs. shear displacement.

slightly lower than the simulated value. This discrepancy is probably due to the SMA connector, which was not simulated. The slope of the measured data matched well with the simulation prediction. Based on the linear relationship between the  $f_{10}$  frequencies and the shear displacement established in figure 4.5(b), the shear deformation sensitivity of the antenna sensor was estimated to be 5.8 MHz/mm. By setting the frequency resolution of VNA as 0.1 MHz, the antenna sensor can easily detect shear displacement as small as 17  $\mu\text{m}$ . For a substrate shear modulus of 385 kPa, the shear stress resolution of the antenna sensor is calculated to be 0.68 kPa. The maximum shear measured at 3 mm of shear displacement was 121.6 kPa.

Here only the antenna sensor with a slot parallel to its length direction is studied. The performance of the antenna sensor with a slot parallel to its width direction should have similar performance. By introducing two slots in the ground plane, shear deformation along the length as well as the width direction of the antenna patch could be measured independently from the  $f_{10}$  and  $f_{01}$  frequencies of the antenna sensor. The effect of pressure on the antenna resonant frequency was not studied in this paper. For in-shoe applications, we plan to implement a pressure sensor underneath the shear sensor. The calibration of the antenna sensor based on the pressure measurement will be a subject of future studies.

#### *4.1.3 Conclusions (shear detection)*

A shear sensor based on microstrip patch antenna technology is presented in this paper. The effect of substrate shear deformation on the resonant frequencies of the antenna sensor was investigated by numerical simulation as well as experiments. We

demonstrated that the antenna sensor can detect shear stress as high as 121 kPa with a resolution of 0.68 kPa.

#### 4.2 Pressure Detection Sensor

The loop antenna pressure sensor consists of three components: a flexible sheet of dielectric substrate, a loop printed on one side of the substrate, and a reflector on the other side of the dielectric substrate (see figure 4.6(a)). The  $S_{11}$  curves of the loop antenna with and without pressure are shown in figure 4.6(c). When a pressure is applied, the loop antenna is brought closer to the reflector, as shown in figure 4.6(b). This essentially increases the capacitance of the resonant circuit and pushes the resonant frequency of the loop towards a lower frequency (Balanis 2005), as shown in figure 4.6(c). The amount of frequency shift depends on the distance  $d$  between the reflector and the loop antenna. Therefore, the distance  $d$  is quantitatively measured from the resonant frequency shift of the loop antenna once the relationship between the distance  $d$  and the antenna resonant frequency shift is established.

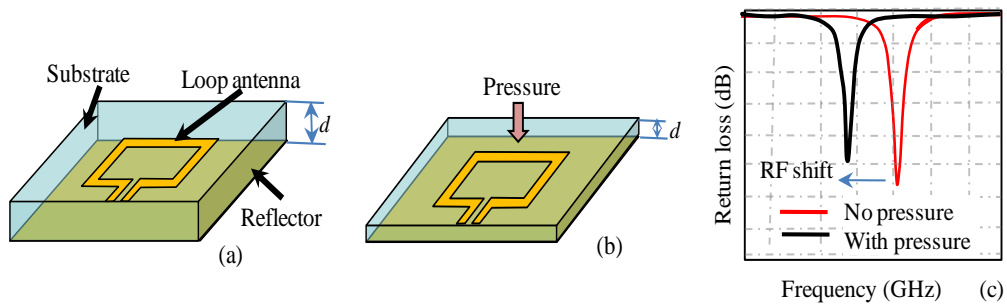


Figure 4.6: Principle of loop antenna sensor for pressure detection; (a) schematic of loop antenna sensor; (b) change in the distance  $d$  due to pressure; (b) effect of pressure on the loop antenna frequency.

#### 4.2.1 Pressure sensor design

There are a few important criteria which need to be incorporated in the design of the loop antenna sensor for in-shoe pressure monitoring. First, the sensor has to be thin, flexible and conformal. In addition, it also has to be durable and able to withstand high pressures. In order to accomplish these tasks, a printed loop antenna sensor was chosen. The dimensions of the loop antenna sensor depend primarily on the frequency at which it operates. At a desired frequency, the radius of the loop  $a$  for a microstrip loop with a circumference of one wavelength can be obtained as (Balanis 2005)

$$a = \frac{\lambda}{2\pi} \quad (4.3)$$

Where  $\lambda$  is the wavelength corresponding to the desired frequency. The width of the microstrip  $b$  is then obtained using the aspect ratio parameter  $\Omega$ ,

$$\Omega = 2 \ln\left(\frac{2\pi a}{b}\right) \quad (4.4)$$

For the loop antenna to be self resonant (i.e., avoid the need for a resonant capacitor) the aspect ratio parameter has to be 12. For a 6.5 GHz loop antenna with an aspect ratio of 12, the radius of the loop and the microstrip width were calculated from (4.3) and (4.4) as 7.2 mm and 0.23 mm respectively. The loop antenna can be interrogated either using a contact or non-contact technique. Since this research is focused on proving the feasibility of antenna sensor to detect pressure monitoring, a contact technique was adopted. A microstrip-line feeding technique was used due to its simple design (Katehi

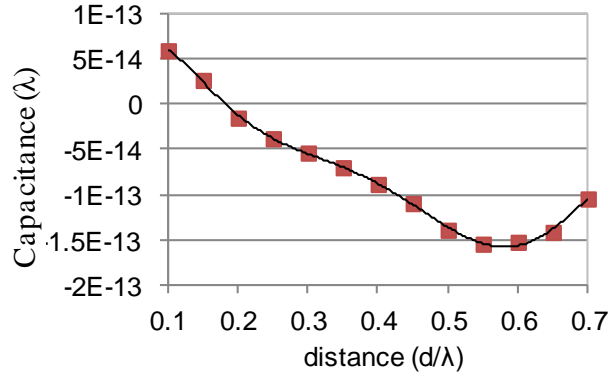


Figure 4.7: Capacitance of the circular loop antenna versus distance from reflector  $d/\lambda$ .

and Alexopoulos 1984). The width of the feed line was taken exactly to the same as the width of loop antenna for a better impedance matching.

Introducing an infinitely large reflector into the vicinity of a loop antenna sensor varies the loop characteristics significantly. The resistance and reactance values for a loop antenna sensor with an infinitely large reflector were reported in the literature (Johnson 1993, Hearn 2001). The capacitance of the loop was then calculated as

$$C = \frac{1}{2\pi f} \frac{\omega L}{R^2 + (\omega L)^2} \quad (4.5)$$

where  $f$  and  $\omega$  are the resonant and angular frequencies of the loop antenna sensor respectively. Therefore, a loop antenna sensor with a high capacitance will have a lower resonant frequency. It was observed that the capacitance of the loop antenna sensor reduces as the distance was increased. In addition, the relationship between the capacitance and distance  $d/\lambda$  had a good linearity between  $0.1\lambda$  to  $0.25\lambda$  (see figure 4.7).

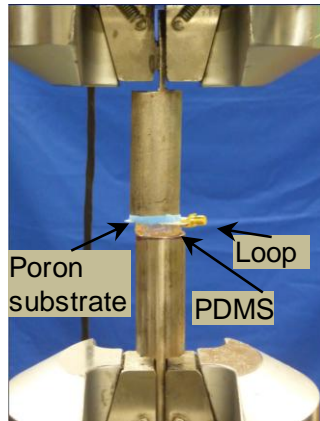


Figure 4.8: Experimental setup for pressure measurement.

Therefore, in order to obtain a linear response, the distance between the loop antenna and the reflector was chosen to be within this range.

#### 4.2.2 Pressure detection experimental Setup

To study the pressure sensitivity of the loop antenna sensor, a Poron<sup>®</sup> substrate with a thickness of  $0.13\lambda$  was placed between the sensor and the reflector. The poron substrate acts as a cushion which gets compressed when pressure is applied on the reflector, thus bringing the reflector closer to the loop antenna sensor. The pressure on the reflector was applied with a closed-loop servo-hydraulic mechanical tester. An additional layer of PDMS<sup>®</sup> substrate was placed below the antenna sensor to imitate the bottom sole of the shoe. The experimental setup to apply uniform pressure over the antenna sensor is shown in figure 4.8. For a uniform pressure distribution over the entire surface of the sensor, two long metal cylinders (1 inch diameter, 6 inch long) were used. The sensor was placed between the two cylindrical bars and pressure was incrementally increased from 0 to 50 psi at intervals of 10 psi. The load was paused at each interval and the  $S_{11}$  parameters of the antenna sensor were measured on a Vector

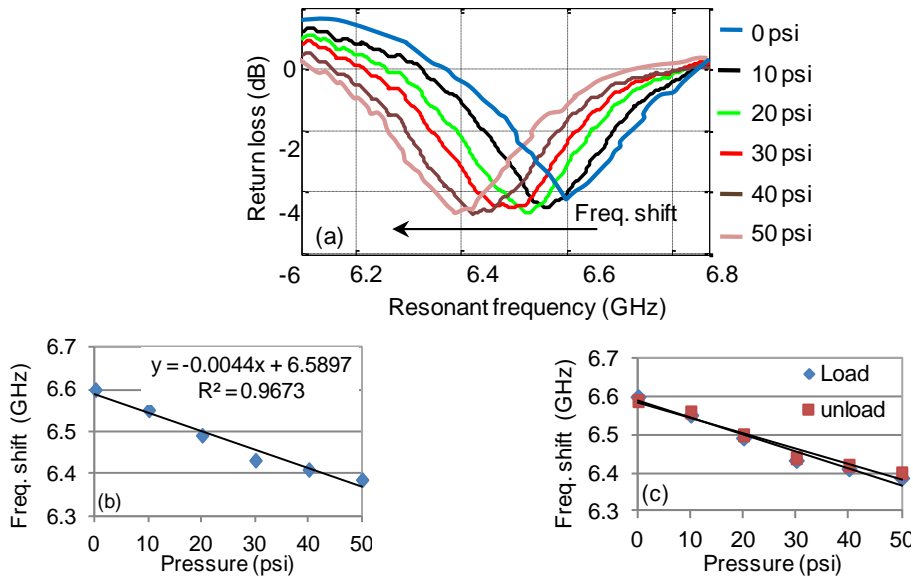


Figure 4.9: Effect of pressure on the resonant frequency of the loop antenna sensor; (a) resonant frequency at various pressure values; (b) resonant frequency shift (GHz) vs. pressure (psi); (c) effect of hysteresis on the loop antenna sensor.

Network Analyzer (VNA). To measure hysteresis of the loop antenna sensor due to Poron substrate, the measurements were repeated by applying cyclic loads between 0 to 50 psi at intervals of 10 psi.

#### 4.2.3 Pressure detection experimental results and analysis

The  $S_{11}$  curves of the antenna sensor at different pressure levels are shown in figure 4.9(a). The right-most curve (blue curve) represents the resonant frequency of the loop antenna sensor when no pressure was applied over the reflector. Each subsequent curve represents the resonant frequency shift with an increase of 10 psi over the reflector. The resonant frequencies as identified from the  $S_{11}$  curves were plotted vs. the pressure are shown in figure 4.9(b). The relationship was almost linear with a sensitivity of 4.4 MHz/psi. Assuming the frequency resolution of the VNA is 1 MHz

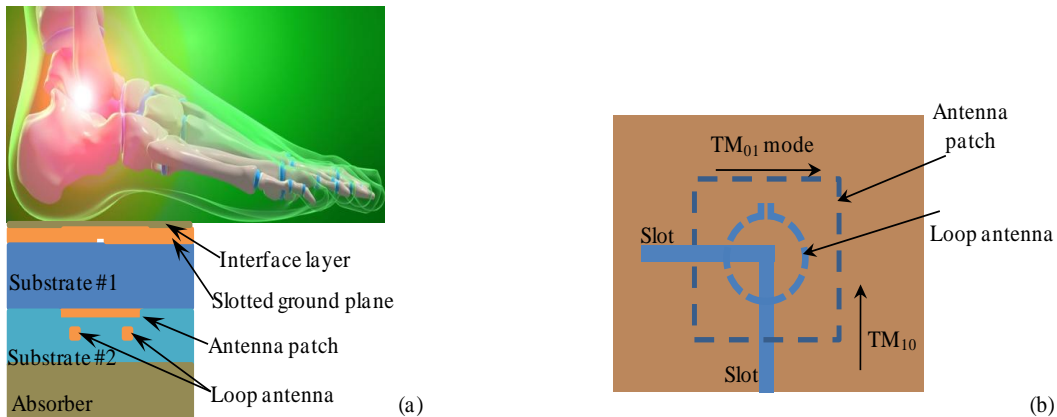


Figure 4.10: Hybrid integration of shear/pressure sensor (not to scale): (a) side view; (b) top view.

(6000 data points over a range of 3 to 9 GHz), pressures as small as 0.25 psi can be effectively monitored with the loop antenna sensor. From repeated loading cycles, as shown in figure 4.9(c), the hysteresis of this loop antenna sensor to cyclic loading was below 0.2%.

#### 4.2.4 Conclusions (pressure detection)

A pressure monitoring sensor based on microstrip loop antenna sensor technology is presented in this section. The interactions between the pressure and the resonant frequencies of the antenna sensor were studied. It was demonstrated that the pressure can be quantitatively characterized with minimal hysteresis by monitoring the resonant frequencies of the antenna sensor.

### 4.3 Implementation of Hybrid Sensor inside Shoe

Since diabetic foot diagnostics requires measuring both pressure and shear at a single location, the two microstrip antenna sensors can be stacked vertically to form a shear/compression sensor. To embed the sensors in a shoe, a layer by layer fabrication

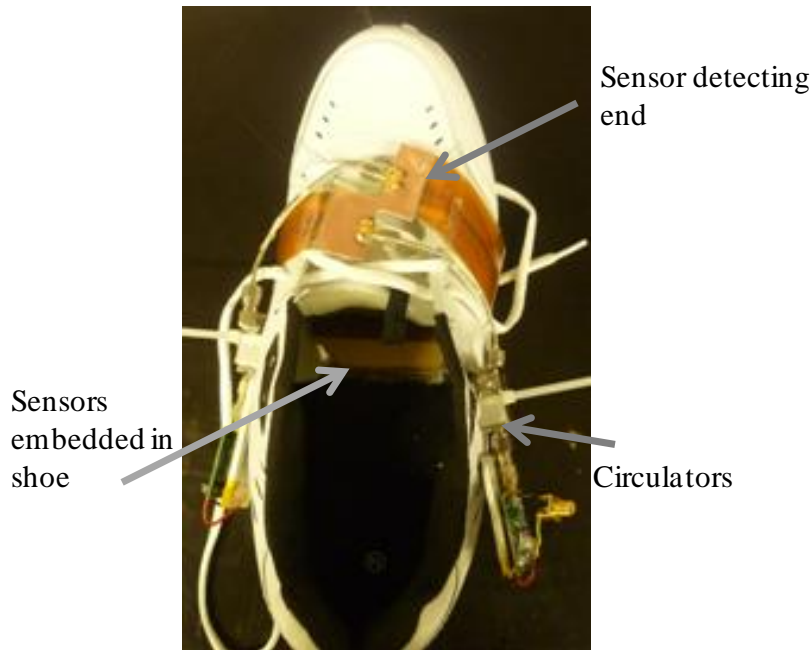


Figure 4.11: Fabricated smart shoe prototype.

technique was developed. The fabrication process starts with bonding a slotted copper film on one side of a 9.5 mm thick poron substrate (substrate #1). Next, the antenna patch and the transmission lines were machined from a copper film and transferred to a Kapton substrate. To ensure a good bonding, the surfaces of the Kapton film were slightly sanded. The Kapton film was then bonded on the other side of poron substrate in such a way that the slot on the copper film is aligned with the center line of antenna patch width direction. The overlapping length between the antenna patch and the slot in the copper film was controlled to be 9 mm. The loop antenna sensor used for pressure sensing was then attached under the shear sensor following the similar procedure. Finally, the bottom of the pressure sensor is supported with a thick PDMS layer. The entire shear/compression sensor assembly was then inserted and glued inside a regular

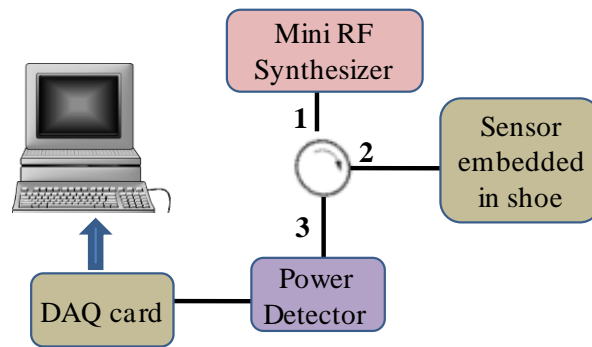


Figure 4.12: Schematic of sensor interrogation principle.

shoe. Prior to inserting the sensors, the insole of the shoe was cut and removed to accommodate the sensor setup (see figure 4.11). The transmission lines of both antenna sensors are wrapped around the shoe to facilitate the interrogation of the antenna sensors. The transmission lines of the pressure and shear sensors are connected to SMA connectors mounted on a Rogers 4350B laminate.

The frequencies of these antenna sensors were measured using wired connection first. As shown in figure 4.12, the sensors were connected to port 2 of a microstrip circulator (Dorado International Corporation, part # 3CMM65-2). A radio frequency synthesizer (Applied Radar, part #AR2010) is connected to port 1 of the circulator to supply RF input to the sensor. The signal reflected by the antenna sensors is routed to Port 3 of the circulator, whose strength is then measured by a power detector (Linear Technology, part # LTC5508ESC6) that converts the RF power to a DC output. If the interrogation frequency is fixed, the return loss of the antenna sensor at this particular frequency will shift as the resonant frequency of the antenna sensor changes. As a result, the strength of the reflected signal changes as well. Therefore, the antenna frequency shift can be

monitored by measuring the DC voltage output of the power detector using an oscilloscope or a data acquisition device connected to a computer. As shown in figure 4.13, the DC output of the power detector changed accordingly with the applied pressure as the sensor was loaded and unloaded by stepping over it.

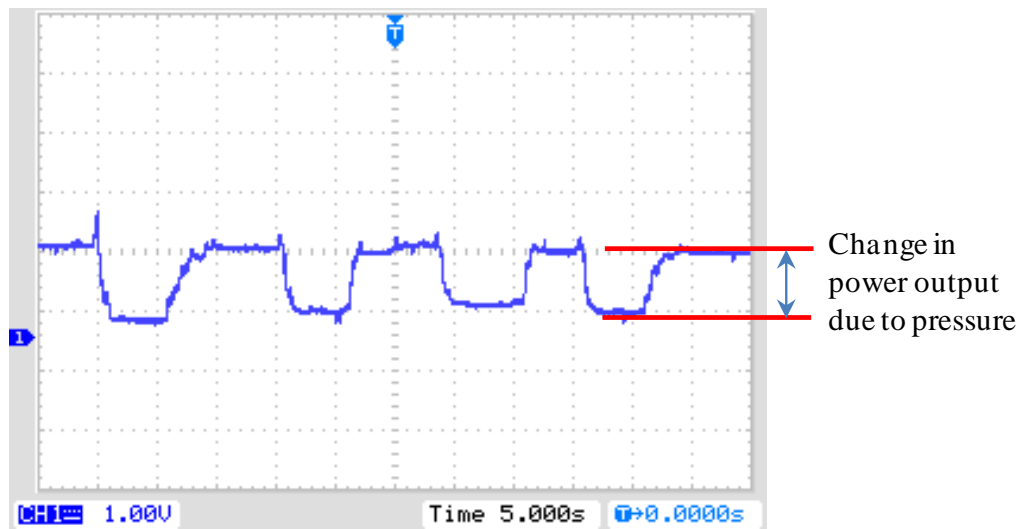


Figure 4.13: Change in power output due to pressure applied on the sensor.

## CHAPTER 5

### CONCLUDING REMARKS

#### 5.1 Crack Detection

A crack monitoring sensor based on microstrip patch antenna technology was investigated. The feasibility of employing patch antenna sensors for monitoring crack propagation and crack orientations was verified through simulations and/or experiments. The capability of the antenna sensor to detect sub-millimeter fatigue crack growth was demonstrated using fatigue cycling of CT specimens. The interactions between the crack and the resonant frequencies of the antenna sensor were studied. During the fatigue experiments, it was observed that the patch antenna sensor was subjected to wear and tear due to high strain transfer from the CT specimen to the bonded antenna sensor. Therefore, we investigated the introduction of a flexible layer between the host structure and the antenna substrate to reduce the strain transfer between the structure and the sensor. We demonstrated the additional a PDMS layer can significantly improve the reliability of the patch antenna sensor.

The effect of crack orientation on the resonant frequencies of the antenna sensor was also investigated. A single parameter, i.e. the normalized frequency ratio  $R$ , is introduced to represent the effect of crack on the two resonant frequencies of the antenna. The change of the normalized frequency ratio  $R$  with the crack growth provides a unique indication of the crack orientation. The experimental results were

validated using numerical simulations. We also discovered that the simulated radiation pattern provides qualitative explanation of the crack-induced frequency shift.

A wireless interrogation technique that can measure the resonant frequency of an antenna sensor that is out of the line-of-sight of the interrogation antenna was investigated. This technique enables the antenna sensor to detect and monitor crack propagation between a lap joint or in other cases where a crack is hidden between two parts of a structure.

### 5.2 Shear/compression Detection

A sensor very similar to the crack detecting patch antenna sensor was evaluated to detect shear deformation. The effects of shear deformation on the resonant parameters of the patch antenna sensor were studied. We demonstrated that the antenna sensor can detect shear stress as high as 121 kPa with a resolution of 0.68 kPa. Since it is important to measure both pressure and shear acting on the foot to understand foot ulcers, a pressure monitoring sensor based on microstrip loop antenna sensor technology was also investigated. The effect of the pressure on the resonant frequencies of the antenna sensor was studied. It was demonstrated that the pressure can be quantitatively characterized with minimal hysteresis.

A prototype of the in-shoe shear/compression sensors was fabricated and the performance of sensors was evaluated using wired connections. The entire sensing and interrogation unit was made of commercially available microwave components. The change in resonant frequency of the antenna sensors due to pressure and shear was monitored.

## CHAPTER 6

### FUTURE WORK

The immediate future work will focus on wireless data acquisition from the in-shoe shear/compression sensors. This will be accomplished by replacing the wired communication with wireless communication devices (e.g. xbee module). The data acquisition circuitry will be attached on the surface of the shoe. The elimination of wires will allow us to collect dynamic data unobtrusively and will also allow the shoe-wearing subject to walk freely. The schematic of wireless data acquisition will be very similar to figure 4.12, except that two xbee devices will be added to the circuit, i.e., one at the DAQ board and another connected to the serial port of computer. Data is then transferred wirelessly via the xbee devices. Due to the size of the components, only a few sensors may be implemented at this stage. However, it will help us understand the feasibility and durability of the embedded sensors. A wireless data acquisition system will enable us to monitor dynamic shear/compression applied over the embedded sensors, which is essential for better understanding of the real-time stresses applied over the foot. Another important aspect of this research would be testing the smart shoe in a clinical setting. Lab experiments or simulations (if carried out) will only provide an estimation of the sensitivity and feasibility of the sensors. Data collection on human subjects in a clinical setting will provide a more accurate evaluation of the sensor parameters.

## REFERENCES

- Abhinav A K 2006 Development and characterization of a high spatial- temporal-resolution-foot-sole-pressure measurement system *M. S. Thesis submitted to Robotics Institute Carnegie Mellon University*
- Abraham J K, Sullivan S and Ranganathan S 2011 Low-cost and disposable pressure sensor mat for non-invasive sleep and movement monitoring applications *33<sup>rd</sup> Annual International Conference of the IEEE EMBS Boston Massachusetts* **11** 4745-4749
- Akhlaghi F 1995 An in-shoe biaxial shear force transducer utilizing piezoelectric copolymer film and clinical assessment of in-shoe sensors PhD Thesis University of Kent Canterbury UK
- Akhlaghi F, Pepper M G 1996 In-shoe biaxial shear force measurement: the Kent shear system *Med Biol Eng & Comput* **34** 315-317
- Appleqvist J and Larsson J 2000 What is the most effective way to reduce incidence of amputation in the diabetic foot? *Diabetes/Metabolism Research and Reviews*, **16** S75-S83.
- Bailey T S, Yu H M, Rayfield E J 1985 Patterns of foot examination in diabetic clinic *Am. J. Med.* **78** 371-374.
- Bakht B, Humar J, Jalali J, Mufti A, Newhook J and Rahman S 2001 Guidelines for structural health monitoring Design Manual

- Balanis C 2005 *Antenna theory: analysis and design, 3<sup>rd</sup> edition* (Wiley Interscience).
- Birke J A, Franks B D and Foto J G 1995 First ray joint limitation, pressure, and ulceration of the first metatarsal head in diabetes mellitus *Foot Ankle International American Orthopaedic Foot and Ankle Society and Swiss Foot and Ankle Society* **16** 277-284
- Boulton A J M, Franks C I, Betts R P, Duckworth T and Ward J 1984 Reduction of abnormal foot pressures in diabetic neuropathy using a new polymer insole material *Diabetes Care* **7** 42-6
- Brandes M, Schomaker R, Mollenhoff G and Rosenbaum D 2007 Quantity versus quality of gait and quality of life in patients with osteoarthritis *Gait & Posture* 1-6.
- Butterworth-Hayes P 2003 “Europe seeks 7E7 work” *Aerospace America*, November, American Institute for Aeronautics and Astronautics, 4-6.
- Carver K R and Mink J W 1981 Microstrip antenna technology *IEEE Trans. Antennas Propagat.*, **AP-29** 1 2-24.
- Chang F K and Ihn J B 2004 Detection and monitoring of hidden fatigue crack growth using a built-in piezoelectric sensor/actuator network: I. Diagnostics *Smart Materials and Structures* **13** 609-620.
- Chang Z and Mal A 1999 Scattering of lamb waves from a rivet hole with edge cracks *Mechanics of Materials*, **31** 197-204.
- Chen J S and Wong K L 1996 A single-layer dual-frequency rectangular microstrip patch antenna using a single probe feed *Microw. Opt. Technol. Lett.* **11** 2 83-84.

- Chen J, Shi Y and Shi S 1999 Noise analysis of digital ultrasonic nondestructive evaluation system *International Journal of Pressure Vessels and Piping* **76** 619-630.
- Ctercteko G C, Dhanendran M, Hutton W C, LeQuesne L P 1981 Vertical forces acting on the feet of diabetic patients with neuropathic ulceration *Br. J. Surg.* **68** 608-614
- Davis B L, Perry J E, Neth D C and Waters K C 1998 A device for simultaneous measurement of pressure and shear force distribution on the plantar surface of the foot *Journal of Applied Biomechanics* **14** 93-104.
- Deshmukh S and Huang H 2010 Wireless interrogation of passive antenna sensors *Meas. Sci. and Tech.* **21** 035201.
- Deshmukh S, Mohammad I, Xu X and Huang H 2010 Unpowered antenna sensor for crack detection and measurement *Proc. SPIE* **7647** 764742.
- Duckworth T, Boulton A J M, Betts R P, Franks C I, Ward J D, 1995 Plantar pressure measurements and the prevention of ulceration in the diabetic foot *The Journal of Bone and Joint Surgery* **67** 79-85.
- Foong C H, Wiercigroch M and Deans W F 2006 Novel dynamic fatigue testing device: design and measurements *Measurement Science and Technology* **17** 2218-2226.
- Garrow A P, Vanschie C H M and Boulton A J M 2005 Efficacy of multilayered hosiery in reducing in-shoe plantar foot pressure in high-risk patients and diabetes *Diabetes Care*, **28** 2001-6.
- Geng Z, Pepper M G and Yan Y 2010 Design and characterization of a single element tri-axial piezoelectric transducer for in-shoe force measurement *Instrumentation and Measurement Technology Conference (I2MTC) IEEE* 1048-1052

- Giurgiutiu V and Bao J 2002 Embedded-ultrasonics structural radar for in situ structural health monitoring of thin-wall structures *Structural Health Monitoring* **3** 121-140.
- Giurgiutiu V and Cuc A 2005 Embedded non-destructive evaluation for structural health monitoring, damage detection and failure prevention *The shock and vibration digest* **37** 2 83-105.
- Grandt A F Jr 2003 *Fundamentals of Structural Integrity* (John Wiley and Sons)
- Hamstad M A, Gallagher A O and Gary J 2002 A wavelet transform applied to acoustic emission signals *Journal of Acoustic Emission* **20** 39-61.
- Hearn C 2001 Electrical design and testing of an uplink antenna for nanosatellite applications *Thesis submitted to Virginia Polytechnic University*
- Hirasawa M, Okada H and Shimojo M 2007 The development of the plantar pressure sensor shoes for gait analysis *Journal of Robotics and Mechatronics* **12** 289-291.
- Hornig T, Tsai M, Chen C and Alexopoulos N G 1994 The influence of metallization thickness on a microstripline-fed patch antenna *Antennas and propagation society international symposium* **2** 940-943
- Hosein R and Lord M 2000 A study of in-shoe plantar shear in normals *Clinical Biomechanics* **15** 57-64.
- Huang H and Paramo D and Deshmukh S 2011 Unpowered wireless transmission of ultrasound signals featured article, *Smart Materials and Structures* **20** 015017
- Hughes R, Rowlands H and McMeekin S 2000 A laser plantar pressure sensor for the diabetic foot *Med. Eng. Phys.* **22(2)** 149-154.

- Huston D, Hu J Q, Maser K, Weedon W and Adam C 2000 GIMA ground penetrating radar system for monitoring concrete bridge decks *Journal of Applied Geophysics* **43** 139-146.
- Johnson R C Antenna Engineering Handbook 3<sup>rd</sup> edition McGraw-Hill
- Kinra V and Vu B 1986 Diffraction of Rayleigh waves in a half-space. II. Inclined edge crack *J. Acoust. Soc. Am.* **79** 1688-1692.
- Ko J M and Ni Y Q 2005 Technology developments in structural health monitoring of large-scale bridges *Engineering Structures* **27** 1715-1725.
- Koktavy P 2009 Experimental study of electromagnetic emission signals generated by crack generation in composite materials *Measurement Science and Technology* **20** 8.
- Kong K and Tomizuka M 2009 A gait monitoring system based on air pressure sensors embedded in a shoe *IEEE/ASME transactions on mechatronics* **14** 358-371.
- Laborde J M 2010 Tendon lengthening for neuropathic foot problems *Orthopedics* **33(5)** 319
- Lebar A M, Harris G H, Wertsch J J, Zhu H 1993 Development of miniature plantar shear force sensing transducer *IEEE Explore* **17** 989-990
- Lee G and Park A E 2008 Development of a more robust tool for postural stability analysis of laparoscopic surgeons **22** 1087-1092.
- Liu Y, Lacher A, Wang G, Purekar A and Yu M 2007 Wireless fiber optic sensor system for strain and pressure measurements on a rotor blade *Proceedings of SPIE* **6770** 67700Y 1-12.

- Lo Y T, Solomon D and Richards W F 1979 Theory and experiment on microstrip antennas *IEEE Trans. Antennas Propagat.* **AP-27** 2 137-145.
- Lott D J, Zou D and Mueller M J 2008 Pressure gradient and subsurface shear stress on the neuropathic forefoot *Clinical Biomechanics* **23** 342-348
- Lu Y, Ye L, Su Z and Huang N 2007 Quantitative evaluation of crack orientation in aluminum plates based on lamb waves *Smart Mater. Struc.* **16** 1907-1914.
- Matsuda Y, Nakano H and Nagai S, 2006 Surface breaking crack evaluation with photorefractive quantum wells and laser generated Rayleigh waves *Applied Physics Letters* **89** 171902.
- Missinne J, Bosman E, Van Hoe B, Steenberge G V, Daele P V and Vanfleteren J 2010 Embedded flexible optical fiber sensor *IEEE Sensors Conference* 987-990
- Mohammad I and Huang H 2010 Monitoring fatigue crack growth and opening using antenna sensors *Meas. Sci. and Tech.* **16** 035201.
- Mohammad I and Huang H 2011 Detecting crack orientation using patch antenna sensors submitted to *Meas. Sci. and Tech.*
- Munk-Stander J 2006 Evaluation of piezoelectric film sensors for in-shoe pressure measurement *Technical report no. 06/04* ISSN: 0107-8283
- Murphy K A and Poland S H 1997 Optic strain and pressure sensors *Proceedings of SPIE* **3044** 352-358
- Murray H J, Young M J, Hollis S and Boulton A J M 1979 The association between callus formation, high pressures and neuropathy in diabetic foot ulceration *Diabetic Medicine* **13** 979-982

- Nanogaki S 1998 *Microlithography fundamentals in semiconductor devices and fabrication technology (Plastics engineering)* CRC Press.
- Nevill A J, Pepper M G and Whiting M 1995 In-shoe foot pressure measurement system utilizing piezoelectric film transducers *Med. and Bio. Eng. & Comput.* **33** 76-81
- Ni C, Shi Y, Shen Z, Lu J and Ni X 2010 An analysis of angled surface-breaking crack detection by dual-laser source generated ultrasound *NDT&E International* **43** 470-475.
- Perry J E, Hall J O and Davis B L 2002 Simultaneous measurement of plantar pressure and shear forces in diabetic individuals *Gait and Posture* **15** 101-107
- Quirk M, Serda J, 2000 *Semiconductor manufacturing technology* Prentice Hall.
- Rana I E and Alexopoloulos 1981 Current distribution and input impedance of printed dipoles *IEEE Trans. Antennas Propagat.*, **AP-29** 1 99-105.
- Rizzo P, Cammarata M, Dutta D, Sohn H and Harries K 2009 An unsupervised learning algorithm for fatigue crack detection in waveguides *Smart Materials and Structures* **18** 11.
- Sadler D J and Ahn C H 2001 On-chip eddy current sensor for proximity sensing and crack detection *Sensors and Actuators A* **91** 340-345.
- Schneider F, Draheim J, Kamberger R and Wallrabe U, 2009 Process and material properties of Polydimethylsiloxane (PDMS) for optical MEMS *Sensors and Actuators* **15** 95-99.

- Sedlak P, Sikula J, Lokajicek T and Mori Y 2008 Acoustic and Electromagnetic emissions as a tool for crack localization *Measurement Science and Technology* **19**
- Shan Q and Dewhurst R J 1993 Surface-breaking fatigue crack detection using laser ultrasound *Applied Physics Letters* **62** 2649-2651.
- Shigeishi M, Colombo S, Broughton K J, Rutledge H, Batchelor A J and Forde M C 2001 Acoustic emission to assess and monitor the integrity of bridges *Construction and Building Materials* **15** 35-49.
- Shin H J and Rose J L 1998 Guided wave tuning principles for defect detection in tubing *Journal of Nondestructive Evaluation* **17** 27-36.
- Skinn D A, Gallagher J P, Berens A P, Huber P D, and Smith J 1994 *Damage tolerant design hand book*
- Smith R A and Hugo G R 2001 Deep corrosion and crack detection in aging aircraft using transient eddy- current NDE *proceedings of 5<sup>th</sup> joint NASA/FAA/DoD conference on aging aircrafts.*
- Talbot D 2003 Boeing's flight for survival *Technology Reviews – MIT Magazine of Innovation*, September, 34-44.
- Tao L, Yoshio I and Kyoko S 2009 A small and low cost 3D tactile sensor for a wearable force plate *IEEE sensors journal* **9** 1103-1111.
- Tappin J W, Pollard J, Beckett E A 1980 Method of measuring 'shearing' forces on the sole of the foot *Clin. Phys Physiol Meas* **1** 83-85
- Tata U, Deshmukh S, Chiao J C, Carter R L, and Huang H 2009 Bio-inspired sensor skins for structural health monitoring *Smart Materials and Structures* **18** 8.

- Titianova E B, Mateev P S, Tarkka I M 2004 Footprint analysis of gait using a pressure sensor system *Journal of Electromyography and Kinesiology* **14** 275-281
- Urry S 1999 Plantar pressure-measurement sensors *Measurement Science and Technology* **10** R16
- Veves, A., Murray, H. J., Young, M. J. and Boulton, A. J. M., “The risk of foot ulceration in diabetic patients with high foot pressure: a prospective study”, *Diabetologia*, 35, 660-663 (1992).
- Volkovas V and Dulevicius J 2006 Acoustic Emission used for detection of crack generation in propellers of turbine-pump units *Russian Journal of Non-Destructive Testing* **42** 248-254.
- Wang W C, Ledoux W R, Sangeorzan B J and Reinhall P G 2005 A shear and plantar pressure sensor based on fiber-optic bend loss *Journal of Rehabilitation Research and Development* **42** 315-326
- Wang W, Ledoux W, Sangeorzan B, Reinhall P 2005 A shear and plantar pressure sensor based on fiber-optic bend loss *Journal of Rehabilitation Research and Development* **42** 315-326.
- Wu S C, Driver V R, Wrobel J S, Armstrong D G, 2007 Foot ulcers in diabetic patients, prevention and treatment *Vascular Health and Risk Management* **3** 65-76.
- Wylie-Rossett J, Walker E A, Shamoan A, Engel S, Basch C, Zybert P 1995 Assessment of documented foot examinations for patients with diabetes in inner-city primary care clinics *Arch. Fam. Med.* **4** 46-50.

- Xu X and Huang H 2012 Multiplexing wireless antenna sensors for crack growth monitoring Proceedings of SPIE Sandiego CA
- Yolken H T 2008 Recent trends in structural health monitoring technologies *The AMMTIAC quarterly* **3** 3-8
- Yu L and Giurgiutiu V 2005 Advanced signal processing for enhanced damage detection with piezoelectric wafer active sensors *Smart Structures and Systems* **1** 185-215.
- Zhang W Y, Ferguson G S and Tatic-Lucic S, 2004. Elastomer-supported cold welding for room temperature wafer-level bonding *IEEE* **7803-8265**: 741-744

## BIOGRAPHICAL INFORMATION

Irshad Mohammad received his Bachelors of Engineering in Mechanical Engineering from Anna University, India in June 2006. He is pursuing his Doctorate in Mechanical Engineering from the University of Texas at Arlington, U.S.A. His research interests include wearable sensors and wireless sensors for structural health monitoring and biomedical applications. During his research work at the Advanced Sensor Technology Laboratory, he has published five technical journals and thirteen conferences papers